Hydrogen-Induced Transformations in Metastable High Entropy Alloys

by

Maria R. Ronchi

Sc.B. Materials Engineering
Brown University, 2019

SUBMITTED TO THE DEPARTMENT OF MATERIALS SCIENCE AND ENGINEERING IN PARTIAL FULFILLMENT OF THE REQUIREMENTS FOR THE DEGREE OF

MASTER OF SCIENCE IN MATERIALS SCIENCE AND ENGINEERING
AT THE
MASSACHUSETTS INSTITUTE OF TECHNOLOGY

JUNE 2021

Signature of Author: _____
Department of Materials Science and Engineering
April 30, 2021

Certified by: _____
C. Cem Tasan
Thesis Supervisor

Accepted by: _____
Frances M. Ross
Chair, Departmental Committee on Graduate Studies

Hydrogen-Induced Transformations in Metastable High Entropy Alloys

by

Maria R. Ronchi

Submitted to the Department of Materials Science and Engineering on May 3, 2021 in Partial Fulfillment of the Requirements for the Degree of Master of Science in Materials Science and Engineering

Abstract

Hydrogen embrittlement (HE) presents a critical challenge to application of structural alloys in hydrogen (H) environments. Recently, development of high-entropy alloys (HEAs) has opened a new avenue for alloy design against HE: not only do some HEAs indicate resistance to HE, but the immense composition spaces associated with these alloys provide endless prospects for tuning composition and corresponding mechanical behavior. In particular, metastable alloys—those that exhibit a mechanically-induced austenite-to-martensite phase transformation—pose an interesting opportunity for HE resistance, where the toughening mechanisms associated with this transformation could counter HE effects under the right conditions. One alloy system, FeMnCoCr, has been previously shown to include metastable alloys which are of special interest due to the high tunability of deformation mechanisms with respect to composition. For example, tuning just the Mn content enables switching between dislocation slip, twinning, and martensite transformation mechanisms. Thus, in this work, we further explore alloys in the FeMnCoCr system to discover H effects and their interactions with metastability.

In the first part of this work, we explore H-induced transformations in one metastable alloy, $Fe_{45}Mn_{35}Co_{10}Cr_{10}$. To this end, we electrochemically introduce H to the samples, quantify the hydrogen evolution by thermal desorption spectroscopy, and observe microstructural transformations by scanning electron microscopy techniques. Through these analyses, we find that the hydrogen induces ε-martensite that preferentially forms in <101> and <111> oriented grains and along Σ3 coincident site lattice boundaries. Further addition of hydrogen induces extension twinning within the martensite. We examine the microstructural factors influencing these transformations to better understand the hydrogen-microstructure interactions.

In the second part of this work, we address the compositional complexity of the FeMnCoCr-H system by developing a method to efficiently screen this composition space for interactions between H and metastability. We apply this method to $Fe_{88-x-y}Mn_{12}Co_xCr_y$ alloys, with a focus on microstructure and H effects. To this end, we first select three alloys using predictions from Thermo-Calc, then produce these alloys by suction casting and apply three thermo-mechanical treatment routes to further vary microstructure. Indentation and scanning electron microscopy are employed to screen for deformation mechanisms and cracking. We identify two particular samples which exhibit extreme cases of indentation response and can provide a starting point for future iterations of this investigation.

Thesis Supervisor: C. Cem Tasan
Title: Thomas B. King Associate Professor of Metallurgy

Contents

1. Introduction

1.1. Hydrogen embrittlement

Hydrogen embrittlement (HE) is a crucial problem for a range of industries that employ structural alloys in hydrogen (H)-containing environments. HE is difficult to avoid due to the abundance of H and its high diffusivity in metals. H sources range from moisture in the atmosphere to storage of high-pressure H [1], and when a small amount of H from these sources percolates into metallic alloys, it can cause embrittlement and subsequent failure. While the problem of HE has been studied for over 1.5 centuries [1], it remains challenging to analyze due to the variety and complexity of H-metal interactions, which are also difficult to observe directly.

H interacts with metals across length scales, from inhabiting interstitial lattice sites to segregating to crack surfaces [2], and causes embrittlement via a variety of mechanisms [3]. Two commonly-cited mechanisms are H-enhanced localized plasticity (HELP) [4–6], in which H assists local deformation near crack tips, and hydrogen-enhanced decohesion (HEDE) [7–9], where H weakens atomic bonding, thus lowering the energy for crack propagation [1]. These phenomena lead to fracture, as reflected (for example) by a decrease in ductility in tensile tests or decreased fracture toughness in fracture mechanics tests employing [3]. Beyond mechanical effects, H also promotes a variety of complex microstructural transformations upon introduction into metallic alloys, such as formation of new phases [10–13], phase transformations [14–19], and dislocation rearrangements [20,21]. Thus, HE becomes a broad, complex field of study: it must be tackled from multiple angles to eventually find solutions for a variety of applications. The following section introduces one toughening mechanism that might be applied to the HE problem, under certain conditions.

1.2. Transformation-induced plasticity

Transformation-induced plasticity (TRIP) is a phenomenon in which an alloy undergoing mechanical loading deforms plastically via a metastable phase transformation. This mechanically-induced transformation is common for alloys exhibiting a metastable austenite phase, which can undergo a diffusionless α' or ε martensite transformation at room temperature upon the application of stress. (The symbols α' and ε refer to body-centered tetragonal (bct) and hexagonal close-packed (hcp) martensite phases, respectively.) TRIP can increase the strength and ductility of metastable alloys due to the associated enhanced strain hardening rate, and has thus been applied to a variety of high-strength steels [22,23].

Such martensite phase transformations during loading can also serve as toughening mechanisms, i.e., transformation-induced toughening, in which mechanically-induced phase transformations at crack tips inhibit crack propagation [24]. Specifically, mechanically-induced γ-austenite to α'-martensite transformation is well-known to increase toughness in steels [25,26]. Unfortunately, in most cases, this mechanism cannot be applied to systems containing H, because γ-austenite to α'-martensite transformation leads to abrupt changes in H solubility, causing micro-cracking at α'-martensite interfaces [27–33].

Although ε-martensite can also enhance cracking in the presence of H [16], recent studies show that some alloys exhibiting an ε-martensite transformation can instead resist HE: ε-martensite can have higher ductility and lower H diffusivity than α', while increasing the capacity for plasticity, which together might render a metastable alloy resistant to H induced cracking [15,34–36]. These phenomena present alternate design routes towards toughening in H environments, where the metastable γ-austenite to ε-martensite transformation may be employed to at once improve ductility and toughness.

1.3. High-entropy alloys and the FeMnCoCr system

High-entropy alloys (HEAs) are alloys consisting of typically 5 or more major metallic elements; therefore, HEAs exhibit high configurational entropy. Assuming atoms occupy random lattice position, the ideal configurational entropy can be quantified by the Boltzmann equation:

$$S = k_B \ln (W)$$

where S is entropy, k_B is the Boltzmann constant, and W describes the number of microstates of a system. Precise definitions for HEAs range from entropy-based to component-based ones [37], but in general, they can be thought of as multicomponent concentrated solid solutions. The interested reader can find a full discussion on definitions and terminology in Ref. [37].

The discovery of the HEA concept—which largely took place in 2004 [38–43]—unleashed enormous opportunities for alloy design, as the broad compositional spaces allow for many degrees of freedom when selecting for desired mechanisms and properties. Early work resulted in the Cantor alloy, equiatomic FeMnCoCrNi [38], which has beneficial mechanical properties such as good ductility at low temperatures [44,45] and indications of hydrogen embrittlement resistance [46,47]. Various other HEAs have been reported to exhibit promising characteristics, including exceptional strength, ductility, and toughness [48], plus good fatigue [49] and creep resistance [50].

Recently, several works on the FeMnCoCr system have revealed interesting mechanical properties within this system [51–56], which have motivated the present work. Not only are there a range of compositions within this system that can form stable fcc solid solutions, but tuning the alloy content enables selection of various deformation mechanisms [52]. In particular, Li *et. al.* showed that varying the Mn content from 45 to 30 at% in an $Fe_{80-x}Mn_xCo_{10}Cr_{10}$ alloy results in switching between dislocation slip, twinning, and TRIP, as well as influencing the phase constitution [52]. TRIP was shown to increase ductility

of dual-phase FeMnCoCr while maintaining a high yield strength, enhancing the strength-ductility tradeoff of this alloy [52].

Thus, the FeMnCoCr system becomes an interesting case for investigating metastable phases and related plasticity mechanisms, especially in the case of TRIP, where a γ-austenite to ε-martensite transformation enhances strain hardening and could provide a toughening mechanism against HE, as discussed above. Yet, the presence of these metastable phases adds a layer of complexity to investigating H effects, as H uptake creates the possibility of H-induced martensite transformation. H reduces the stability of γ-austenite against martensite, which can both promote martensite transformations during loading [17] and cause martensite to form in the absence of external loads [57]. These H effects have been well-investigated for stainless and high-Mn steels, for which H-induced martensite is prevalent [14,15,64–72,16,17,58–63]. When H is introduced into these metastable alloys, it significantly decreases the stacking fault energy (SFE) [73–77], which promotes ε-martensite formation [16,76]. Martensite transformation is known to proceed once a critical H content has been achieved [17,57], and the driving force is generally attributed to the concentration gradients associated with non-equilibrium introduction of H [14,57,78]. While these studies address the relationship between H content, mechanical loading, and H-induced martensite, we wish to clarify the effects of microstructural features and H trap sites on martensite transformation in the absence of external loads.

Thus, in the first part of this work (Chapter 3), we analyze H effects in an FeMnCoCr high entropy, $Fe_{45}Mn_{35}Co_{10}Cr_{10}$, whose metastable austenite-martensite transformations have been studied without H [54,55]. We focus specifically on H-induced microstructural transformations in this alloy, in the absence of mechanical loading. To that end, we combine electrochemical H charging, thermal desorption spectroscopy, and scanning electron microscopy techniques to study these transformations at room temperature. Our investigations reveal insights regarding the contributions of microstructural features to H-induced martensite and twinning.

1.4. High-throughput alloy design

While the immense compositional space presented by HEAs yields exciting opportunities for alloy design, it also presents a challenge to conventional metallurgical alloy design routes. While typical alloys can be explored by systematically varying composition by small steps, this becomes impossibly time-consuming in the case of HEAs, which, e.g. in the case of the Cantor alloy, present a 5-dimensional composition space. The effects of thermal-mechanical processing on the subsequent alloy properties only increases the degrees of freedom by which these compositions may be characterized. Thus, it becomes necessary to develop high-throughput (HT) methods, by which these composition spaces can be screened for promising compositions in an efficient manner.

Using a bottom-up approach, many researchers have accomplished HT screening of a given composition space by producing diffusion multiples, graded powder specimens, or sputtered compositional spread islands [79–85]. Here, an array of compositions can be probed for crystal structure or mechanical properties on a small scale, such as with nanoindentation [79]. Meanwhile, others have developed high-throughput methods by additive manufacturing [86–89], or novel techniques such as *in-situ* melting [90]. While these methods promote efficient collection of data for a large array of compositions, they are not directly applicable to the properties of bulk alloys, due to the limited length scale from which these properties are measured [91]. This discrepancy can be bridged partly by increasing material volume while still using a fast characterization method such as indentation [92–94], or an engineering approach can be taken to producing bulk alloys quickly. Recently, Springer *et. al.* pioneered a solution to HT bulk alloy screening, “rapid alloy prototyping” [95]. With this method, they were able to successfully screen tensile and hardness properties for 45 material states (5 compositions x 9 thermal treatments) in 35 hours, which the authors estimate to be a time advantage by a factor of 6-10 over

conventional bulk alloy design [95]. Several other studies have utilized this method successfully [96–98], typically by varying composition and thermal processing systematically to screen for a range of properties.

In the second part of this work (Chapter 4), we design a HT method appropriate for the scale of an academic research laboratory and apply it to the FeMnCoCrH system. With this method, we intend to increase efficiency by decreasing the number of samples necessary to iteratively search a composition space. Furthermore, because H adds so much complexity to this system (as will be seen in Chapter 3), we require a method that will allow systematic comparisons of metastability and HE effects. These goals are approached with a focus on (1) Calculation of Phase Diagrams (CALPHAD)-informed composition selection for microstructural variation, and (2) "binary" testing which can yield "yes/no" data. For this study, we first narrow the composition range to $Fe_{88-x-y}Mn_{12}Co_xCr_y$, in order to search for alloys that are possible to process at large scales (e.g. the Mn content overlaps with that of medium-Mn steels), while maintaining a reasonably high Mn content to promote retained austenite during processing [99,100]. The Co and Cr contents are limited to 5-15 at% to reduce cost compared to near-equiatomic FeMnCoCr alloys. We employ Thermo-Calc, a CALPHAD software, to choose compositions that we expect will yield a variety of microstructures and phase transformation behaviors. Because microstructures dictate final mechanical properties—rather than composition alone—this method may allow for a greater range of properties to be screened with fewer compositions. Second, after producing the selected FeMnCoCr alloys, we employ three sets of micro-indentation to screen for deformation mechanisms and cracking before H charging, after H charging, and after 24 hours of outgassing. We use the results of these tests to identify particular specimens that can serve as a starting point for future iterations, due to their unique indentation responses.

2. Methods

2.1. Sample production and preparation

The mechanistic study on H-induced phase transformations (Chapter 3) employs an $Fe_{45}Mn_{35}Co_{10}Cr_{10}$ HEA produced by methods similar to those below, but the specific parameters are described in detail elsewhere [54]. For the HT method study (Chapter 4), three FeMnCoCr alloys with varying Co and Cr contents were produced in-house as described below. All samples were generally prepared by the same techniques.

Samples are produced by arc melting, in which an electrical arc is employed to melt raw elements under an inert argon atmosphere. The inert atmosphere is used to avoid introduction of impurities into the sample, such as oxygen and nitrogen; to achieve a pure argon atmosphere, the chamber of the arc melter is pumped down to a pressure of 5E-2 mbar and flushed with argon three times, before re-introduction of pure argon. A pure titanium getter is melted before applying the arc to the sample, to absorb any remaining oxygen in the chamber. Then the samples are melted with an arc of 300-400 A, while the copper crucible is continuously water-cooled. The samples are flipped and re-melted at least 5 times to minimize elemental segregation due to gravity. Finally, the button-shaped samples are cast as rectangular bars by re-melting the samples over a suction-casting mold. Once the samples melt and begin entering the mold, suction is applied to the bottom of the mold by opening the previously vacuum-pumped tanks on the arc melter. This method reduces the formation of shrinkage cavities while producing a sample shape suitable for further thermo-mechanical processing.

Samples are further homogenized by first cold-rolling, then heating at elevated temperatures. Rolling the samples introduces severe plastic deformation, and the resulting stored energy of cold work drives atomic rearrangement during heating, thus catalyzing the homogenization process. Specifically, the samples discussed in Chapter 4 are cold-rolled to a 40% reduction in thickness, then homogenized at

1100°C for 3 hours. Because this extended heat treatment results in samples with very large grains (and therefore decreased strength, by the Hall-Petch effect), these samples are cold-rolled to 40% reduction in thickness a second time before heating at 900°C to drive the recrystallization process. Here, grains nucleate and grow within the heavily deformed structure, resulting in a finer grain morphology, where grain size will increase with time.

Samples are cut from the final heat-treated bars by either electron discharge machining (EDM) or using an abrasion saw. EDM is used to cut small, thin samples while minimizing damage to samples: a wire provides rapid electrical discharge (sparks) which effectively cuts the specimen while losing only tens of micrometers of material. While the abrasion saw causes loss of about 2 mm, it provides a quick method for simple cuts, and thus is employed for the HT method.

After cutting, samples are mounted on pucks with acrylic or super-glue (media that dissolve in acetone) and ground with 320, 400, 600, 800, and 1200 grit SiC sandpaper to remove the damaged surface layer. Then they are polished with 3um and 1um diamond suspension, and finished with an OPS or OPU (colloidal silica suspensions) to remove diamond suspension scratches. All samples that will be subjected to electrochemical H charging are polished on both sides.

Hydrogen is introduced to samples electrochemically. Samples are suspended in an electrolyte (5% NaCl + 3 g/L NH_4SCN_3) along with a platinum counter-electrode, while current is applied from a current-controlled power source. During this process, the NaCl promotes production of atomic H which can be adsorbed onto the metal surface via either of the following chemical reactions in solution [101]:

$$H^+ + e^- \rightarrow H_{ads}$$

$$H_2O + e^- \rightarrow H_{ads} + OH^-$$

After adsorption, adsorbed H atoms can either recombine with other H atoms and return to solution, or become absorbed into the bulk of the material. The NH_4SCN_3 acts as a recombination poisoner, to inhibit the H atoms from re-combining.

2.2. Microstructure characterization

2.2.1. Scanning electron microscopy and related techniques

Scanning electron microscopy (SEM) presents a powerful tool for taking high-resolution images of sample surfaces with a large depth of field, and SEM-based techniques are the primary mode of microstructural analysis in this work. The SEM is equipped with an electron gun which focuses an electron beam on the sample. Electrons interact with the sample to produce a variety of signals, which are then captured by the appropriate detectors and mapped with position [102]. Secondary electrons (SE) and back-scattered electrons (BSE) are used for producing images; the contrast from both can display topographical features, while the contrast differences from BSE can be used to identify varying phases/compositions (brighter regions correspond to higher atomic number, due to a higher intensity of backscattering) [102]. Composition can be mapped exactly using an X-ray detector for energy dispersive spectrometry (EDS), where the energy of the scattered X-rays can be used to identify elements with atomic number higher than 5 [102]. These composition maps can be compared directly to SE and BSE images to correlate composition to microstructure.

To map specific crystallographic information, electron back-scattering diffraction (EBSD) is employed. An EBSD detector captures the angular spread associated with the BSE intensities at each point, in order to map Kikuchi patterns which directly correspond to crystal structure [102]. In this work, we use EBSD mapping before and after H charging to reveal phase, orientation, and defect density information. We employ a Tescan MIRA3 SEM with an EDAX Hikari EBSD camera for this data acquisition.

2.2.2. X-ray diffraction

X-ray diffraction (XRD) is used to identify phase constitution for the FeMnCoCr samples produced for the HT screening study, since this method is faster than EBSD and detailed crystallographic information was not required. XRD involves focusing an X-ray beam on a sample at varying angles and collecting diffracted beams to map the intensity of diffraction versus the diffraction angle (2θ). The resulting high-intensity diffraction peaks follow Bragg's law:

$$n\lambda = 2dsin\theta$$

where n is an integer relating to the order of reflection, λ is the wavelength of the X-ray beam, d is the spacing between crystal planes at the point of data collection, and 2θ is the angle of diffraction [103]. Thus, given the diffraction parameters, crystallographic information can be determined. Databases of XRD patterns are used to quickly match XRD data with known phase structures, so that identification is largely automated. Phase fractions are calculated from the relative areas under diffraction peaks.

In this work, we employed a Bruker D8 Discover machine equipped with a Vantec2000 2D detector and a General Area Detector Diffraction System, operating with a Co source; the Co source (λ=1.790Å) mitigates fluorescence from Fe and Co containing samples to increase accuracy [104]. XRD data was collected for angles ranging from 15 to 120 degrees. Data was analyzed with Highscore Plus software, using Reitveld fitting to determine phase fractions.

2.2.3. Thermal desorption spectroscopy

Thermal desorption spectroscopy (TDS) is a method used to determine H content and H trapping sites in a sample. H desorption is measured with a mass spectrometer while the sample is heated at a continuous rate, to obtain a plot of H desorption rate versus temperature. At lower temperatures (e.g. near 400 K in some steels [105]), an initial peak indicates diffusible H de-trapping from weak trap sites such as grain boundaries and surfaces. Peaks at higher temperatures will correspond to de-trapping

from increasingly stronger trap sites; the activation energy of de-trapping, E_a, can be calculated by the following equation:

$$\frac{\partial \ln\left(\varphi/T_p^2\right)}{\partial\left(1/T_p\right)} = -\frac{E_a}{R}$$

where φ is the fugacity coefficient, R is the gas constant, and T_p is the temperature at the desorption peak. Meanwhile, peak height reflects the desorption rate-determining mechanism, e.g. typically lattice diffusion for weak trap sites and de-trapping rate for strong trap sites [3].

In this work, an $Fe_{45}Mn_{35}Co_{10}Cr_{10}$ sample was heated at a rate of $5K \cdot min^{-1}$ in the vacuum SEM chamber, where a residual gas analyzer (RGA) unit from MKS Instruments was used to collect H desorption information. The sample was heated *in-situ* with a heating module from Kammrath & Weiss; the general setup is displayed in Figure 1(a). The H desorption profiles were deconvoluted with a Voigt peak function, as shown in Figure 1(b).

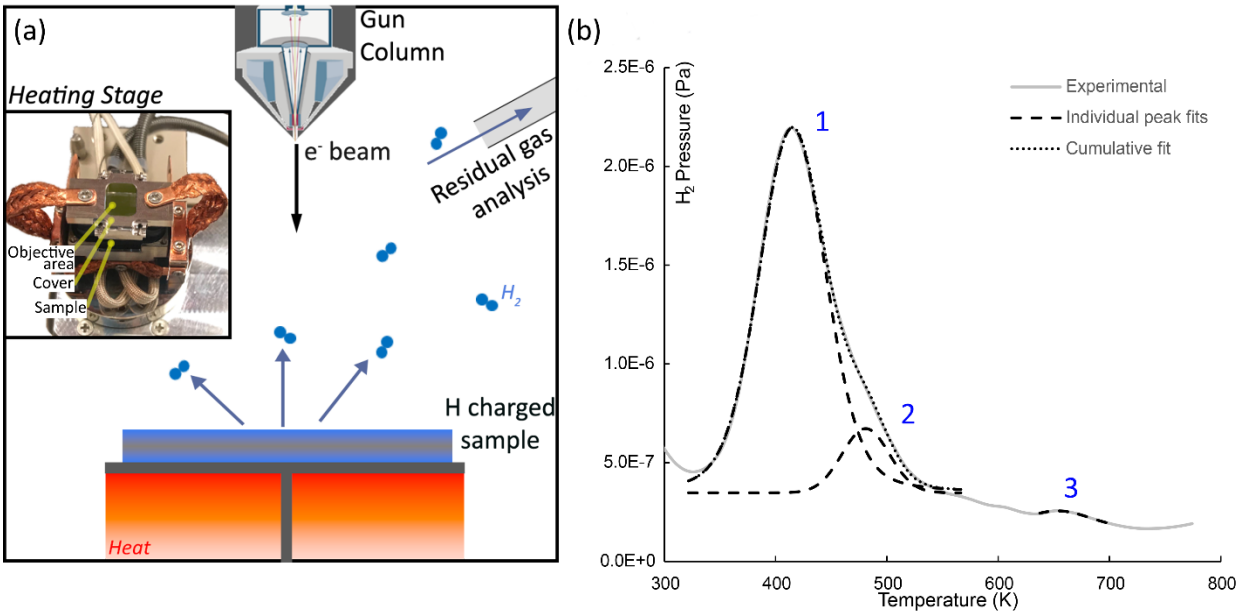

Figure 1. a. Schematic of the integrated SEM-TDS method. Residual gas analysis is conducted simultaneously to heating the H-charged sample. b. TDS from a sample H charged for 106 hours.

2.3. Mechanical property characterization: Vickers micro-indentation hardness testing

The primary method used for mechanical property characterization in this work is Vickers micro-indentation, which is used to determine the hardness of the material. This method involves pressing a tetrahedral diamond indenter tip into a polished sample surface at a pre-determined force for a specified dwell time, here 300 gf (2.94 N) and 15s. Using the known indenter geometry, where the tetrahedral pyramid is defined by a 136° angle between opposite faces, the area of indentation can be calculated from the measured diameter of the indent, and thus related to stress; hardness, HV, is calculated with the equation

$$HV = 1854.4 * F/d^2$$

where F is the applied force (gf), and d is average diameter (i.e. the average length of the square indent diagonals, in μm) [106]. HV relates linearly to yield strength [107], and thus this method offers a quicker test for relative strength than tensile testing. Additionally, the indentation stress results in deformation features about the indent that can be identified by SEM, in order to scan for deformation mechanisms. For this work, each measurement included five indents for statistical accuracy, spaced apart by 3x the indentation width to avoid the effects of hardening from adjacent indents.

3. Hydrogen-induced microstructural transformations in an FeMnCoCr alloy

3.1. Results

3.1.1 Hydrogen-induced martensite transformation

The EBSD phase maps of a representative $Fe_{45}Mn_{35}Co_{10}Cr_{10}$ sample are shown in Figure 2(a-c), at increasing H charging times of (a) 0 hours, (b) 55 hours, and (c) 106 hours, each at a charging current density of 10A/m^2. It is apparent that in the samples investigated, H charging alone (without straining)

induced a γ-austenite to ε-martensite phase transformation. The martensite fractions were calculated from EBSD scans of the same 400 μm view field after each charging step, excluding points with a confidence index lower than 0.02. Note that after H charging, only light polishing was performed to avoid further transformation. Thus, some corrosion products were still present in EBSD scans (as represented with black points in Figure 2(b)). These data points were excluded when calculating martensite fractions. The evolution of martensite fraction with H charging time is quantified and represented in the inset in Figure 2(c). Longer charging times resulted in an increase of martensite, with the fraction of martensite rising from 0.2% to 22% over the course of 106 hours of charging.

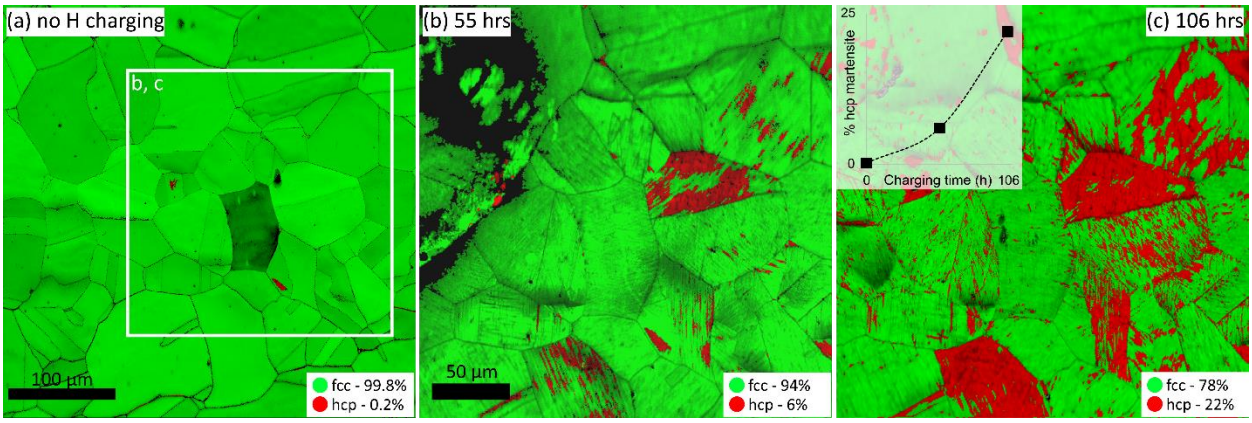

Figure 2. EBSD phase maps of a single sample, with a grayscale image quality overlay, (a) as-homogenized, (b) after 55 hours of H charging, (c) after 106 hours of H charging. Black pixels represent points of the EBSD scan with a confidence index lower than 0.02, including a corroded area in (b). The inset in (c) shows the increase of martensite fraction with charging time.

To evaluate the extent of the martensite transformation below the surface, we repeatedly fine-polished the sample and took SEM BSE images of the same multiphase region after each polishing step (Figure 3). To calculate the amount of material removed at each step, we placed Vickers indents on the sample and measured the change in indent diagonal length, which is related to the indent depth by a geometrical constant [108]. In BSE images, ε-martensite bands can be recognized by a difference in contrast with respect to the matrix. In this case, the brighter-contrast bands represent martensite, while the dark contrast of the matrix represents austenite, as verified by the fine EBSD scan shown in Figure

3(a_1). While there is some contrast change in each step due to slight fluctuations in surface orientation after polishing, we minimized error in this respect by maintaining the same BSE image parameters at each step (e.g. working distance, tilt angle, and channeling contrast). We also verified the identity of the bright-contrast bands a second time after removing 5 µm of surface material. Thus, we utilized the distinction in austenite/martensite contrast to estimate the fraction of martensite at each step. The fractions were calculated by first thresholding the BSE images, then counting the bright and dark pixels. (Polishing-induced pores and streaks were removed from the image beforehand for accuracy.) Although some error remains in the calculations from contrast fluctuations, Figure 3(d) shows that, overall, the martensite fraction decreases with depth into the sample. The martensite mostly disappears after 12 µm, at which point any remaining martensite features are finer than 0.7 µm.

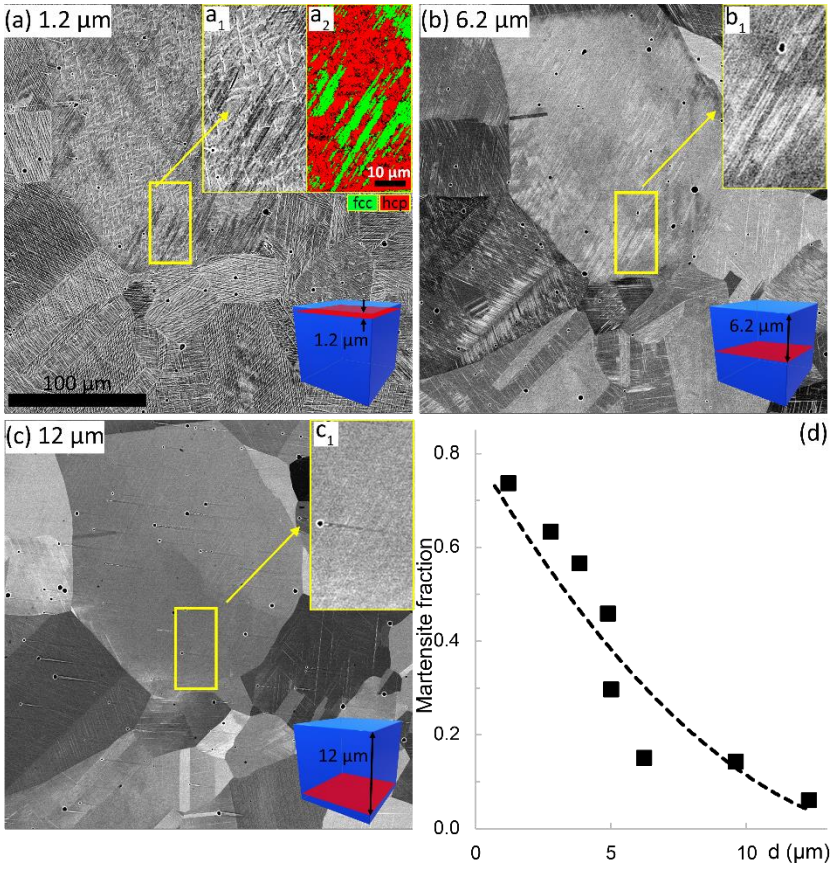

Figure 3. (a-c) Three representative layers of a sample H charged for 106 hours and subjected to serial sectioning by polishing. BSE images correspond to depths of (a) 1.2 µm, (b) 6.2 µm, and (c) 12 µm from the original surface of the sample. Insets (a_1, b_1, c_1) highlight the decreasing martensite fraction, where bright

contrast represents martensite bands; this correlation is verified by comparing (a_1) to the EBSD scan in (a_2). (d) The martensite fraction calculated from the SEM BSE images at each polishing step.

3.1.2 Hydrogen-induced martensite: microstructural correlation

In order to draw insights regarding the mechanism of H-induced martensite transformation, we evaluated several microstructural features identified by the EBSD scans before and after 55 hours of H charging. We chose to analyze grain orientation, average misorientation, and diameter, as these could all impact H uptake and martensite transformation. Grain orientation could affect H diffusion rate, as seen in polycrystalline 304 SS in a gaseous H environment [109], as well as Ni single crystals undergoing electrochemical H charging [110]. Average misorientation, which reflects geometrically necessary dislocation (GND) density, could also affect H diffusion because dislocations can act as H trap sites [7,111]. Finally, grain size could limit the ability for a given grain to accommodate martensite transformation [112].

We first present the effects of grain orientation on H-induced martensite transformation in Figure 4(a-b). Figure 4(a) is an image quality (IQ) map of the same region shown in Figure 2(a), before H charging; different shades of gray represent different grains, and GBs are darker due to lower IQ. Every grain in Figure 4(a) that proceeded to show at least a 10% martensite transformation (by area fraction) is highlighted in red, based on the percent of martensite transformation in each of these grains after 55 hours of H charging. The corresponding grain orientations of the "red grains" are also highlighted in the inverse pole figure (IPF) in Figure 4(b). The IPF reveals that all grains that form >10% martensite after 55 hours of charging are within 10 degrees of the <111> and <101> type grains (except for one partial grain at the edge of the EBSD scan, which is disregarded due to lack of information). Here, grain orientation is referenced to the sample normal, i.e. [001].

Although the martensite-forming grains were all within 10 degrees of the <111>-<101> type grains, several grains within this orientation range did not form any martensite; these grains are highlighted in blue in Figure 4(a). We statistically examined the differences in these two categories of

grains by quantifying the average grain misorientations and grain diameters (Figure 4(c)), based on the EBSD scan before H charging. The ranges of these attributes overlap, but, considering the averages of each (marked by X's in the box-and-whisker plots), the grain misorientation is on average lower for martensite-forming grains (red) than those that do not form martensite (blue), and the grain diameter is on average smaller for the latter.

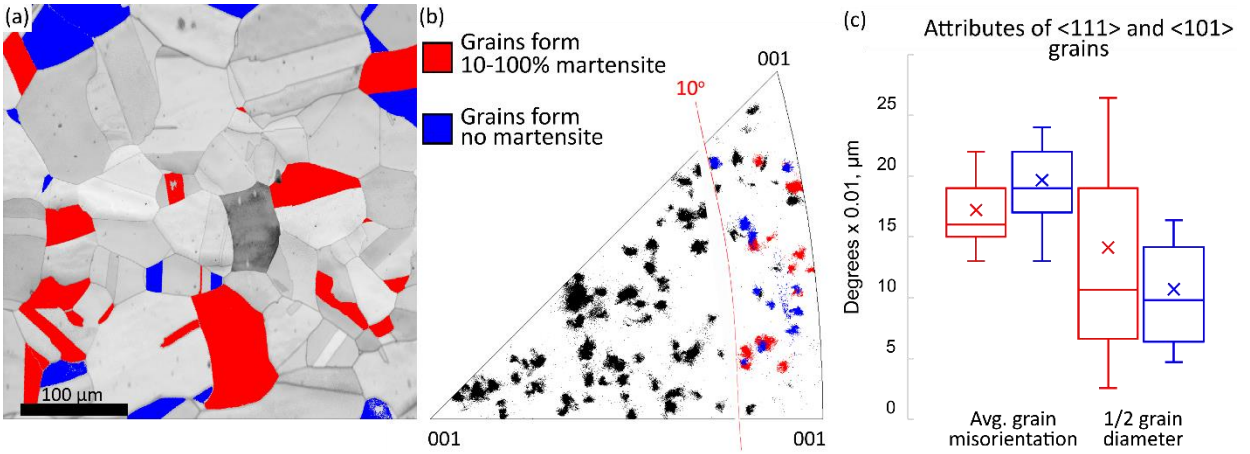

Figure 4. (a) IQ map of an as-homogenized sample. Grains that transformed to martensite by 10-100% after 55 hours of H charging are highlighted in red, and grains from the same orientation range that did not form martensite are highlighted in blue. The orientations of the red and blue grains are also highlighted in (b), an inverse pole figure representing all of the orientations in (a). The average grain misorientation and grain diameter corresponding to the highlighted grains are plotted in (c) as box-and-whisker plots.

Finally, because GBs can have a strong effect on hydrogen segregation and martensite nucleation (see Discussion) [113–116], we analyzed the correlation of martensite to GBs in the sample that was H charged for 55 hours. We focused on coincident site lattice (CSL) boundaries, which have been proposed to exhibit unique H trapping behavior in related alloys [117], and high-angle grain boundaries, which can provide a high density of interstitial H trapping sites [113]. Figure 5(a) shows an IQ map of the sample (corresponding to Figure 2(b)), with the martensite phase highlighted in red, and Σ3 boundaries in blue. Σ3 boundaries are coherent coincident site lattice (CSL) boundaries arising from fcc twins, which are annealing twins in this material. Other CSL boundaries in the sample were not relevant to the analysis (i.e. one Σ5 boundary in an austenitic region). We analyzed the martensite-GB correlation as follows. For each region of martensite, we measured the length of every austenite-martensite phase boundary, then

classified it into one of the following categories: (1) boundaries that correspond to Σ3 austenite boundaries before introducing H, (2) boundaries that correspond to random austenite GBs before introducing H, and (3) boundaries that are within austenite grains, and thus do not correspond to any austenite GBs. None of the random GBs from (2) were low-angle GBs (with a misorientation <5°), and overall 95.5% of them had a misorientation over 25°. This boundary correlation was verified with the EBSD map of the austenite boundaries before H was introduced, as the martensite overtakes several of the Σ3 boundaries once H is present, making the post-H EBSD map challenging to use for this analysis. In Figure 5(c), the relative lengths of boundary types (1) and (2) are compared to the total relative lengths of Σ3 and other high-angle GBs in the same region before H charging. These results reveal that martensite borders more Σ3 boundaries than random high-angle GBs, despite the fact that, overall, there were more high-angle GBs than Σ3 boundaries available in the region before H charging. Finally, it is observed that most of the larger martensitic features border multiple GBs, making nucleation analysis challenging. However, we note several martensite regions which are small enough to enable deduction of the nucleation site. Two examples are shown in Figure 5(b), indicating that nucleation of martensite on Σ3 boundaries can occur.

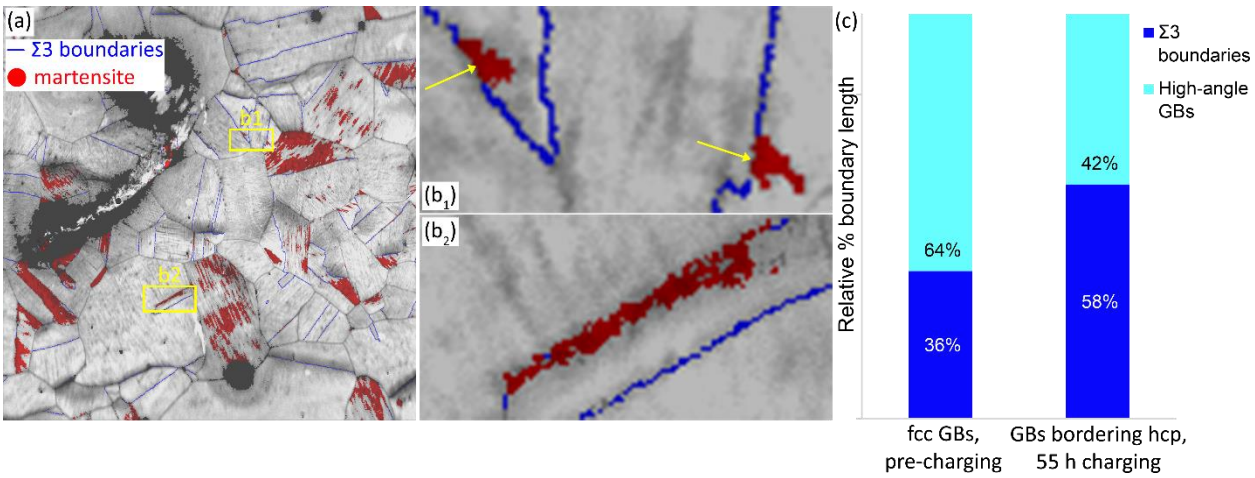

Figure 5. (a) IQ map of the sample H charged for 55 hours (corresponding to Figure 2(b)), showing the martensite phase in red and the Σ3 boundaries in blue. (b) Some small martensite regions that appear to only contact one GB, which are Σ3 boundaries. (c) Relative % boundary length is plotted for Σ3 boundaries

and high-angle GBs, to compare (i) the boundary ratios in the as-homogenized fcc material, pre-charging, and (ii) the ratio of boundary types bordering H-induced martensite.

3.1.3 Hydrogen-induced twinning

Upon closer examination of the micrographs in Figure 3(a_1), a fine ellipsoidal shaped feature becomes apparent. These features (shown at higher magnification in Figure 7(a)) are present within the martensite phase; these formed in all samples after 106 hours of H charging. Figures 6(a) and 6(b) show an IQ map for a sample charged for 106 hours, with the ellipsoidal features in martensite highlighted in red (see the corresponding phase map in Figure 2(c) for reference). The line profile shown by the blue arrow in 6(b) and plotted in (6)c confirms that these features are hcp twins, specifically $\{10\bar{1}2\} < 10\bar{1}1 >$ twins, with a characteristic misorientation angle of 86° about $< 1\bar{2}10 >$ [118]. Line profiles were taken across several other twins to confirm this observation. These twins are induced solely by the addition of a large amount of H: no external stresses were applied to the samples.

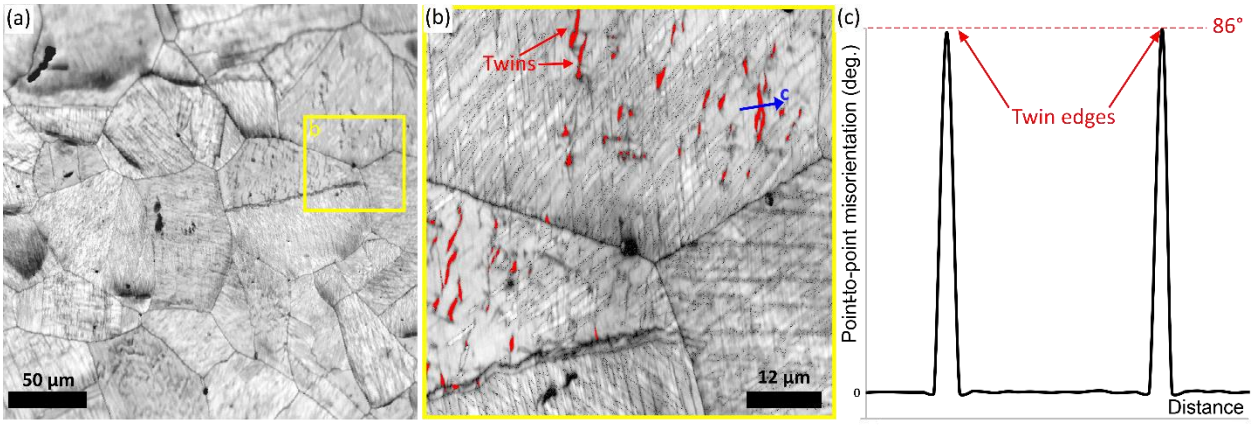

Figure 6. (a) IQ map of a sample H charged for 106 hours. (b) Enlarged region, with H-induced twins highlighted in red. The line profile along the blue arrow is plotted in (c). (c) Point-to-point misorientation across an H-induced twin, demonstrating a misorientation of 86^0 at the twin boundaries.

A second sample with higher twin density was used to confirm whether any other common hcp twin variants could form in this material. The sample was first pre-strained to 15% to induce a total of 26% martensite on the surface (measured by EBSD), then H charged for 55 hours, which increased the martensite fraction to 76%. A total of 4% of this martensite was twinned, compared to only 0.08% in the

sample presented in Figure 6. Even at this increased twin density, no other twin variants were observed besides the $\{10\bar{1}2\}$ twins.

We evaluated the extent of twinning below the surface of the unstrained sample with the same repeated fine polishing as described in section 3.1. As shown in Figure 7, the twins (ellipsoidal features with the brightest BSE contrast) were well-defined at the sample surface (7(a)) but became less well-defined with increasing depth (7(b)), and fully disappeared after a depth of 5 μm (7(c)). Several other random areas across the sample surface (~ 50 mm^2) were checked thoroughly to ensure all twins had disappeared at a depth of 5 μm: multiphase regions (as identified by bands of differing contrast) were checked for fine features representing local deformation, such as the brightest features in Figure 7(b).

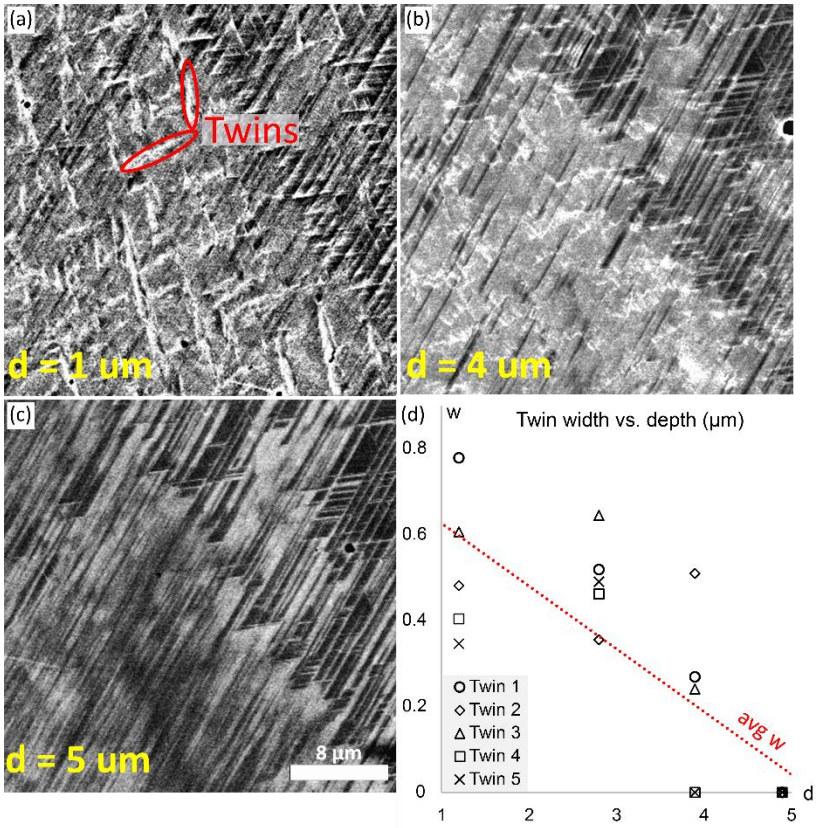

Figure 7. (a-c) SEM BSE images showing a single region of a sample H charged for 106 hours, taken at d=1 μm, 4 μm, and 5 μm during serial sectioning by polishing. The brightest contrast in (a) and (b) represents twins in the martensite, while the darkest contrast represents austenite. The bright contrast in (c) represents martensite without any twins. (d) Twin width vs. depth, plotted for five individual twins, each represented by a separate symbol. The red dotted line represents the global average trend.

To quantify the relation between twin width and sample depth, we calculated the approximate widths of 5 distinct twins using the BSE images at each polishing step as follows. We took a line profile across each twin in each image using ImageJ, plotted the gray values versus distance, and measured the full width at half maximum (FWHM) of the peak corresponding to each twin. These values are plotted in Figure 7(d), with different symbols for each twin. On average (as noted by the red dashed trendline), the twin widths decrease with depth. Although there is some variation in width for individual twins, all twins disappear by 5 μm.

3.1.4 Hydrogen-induced twinning: microstructural correlation

For the same 106-hour charged sample shown in Figure 6(a), Figure 8(a) highlights the martensite regions that formed twins: while only martensite regions formed twins (as opposed to austenite), not all martensite formed twins. While many of these twins appeared to be located in the midst of a martensite region, the fine EBSD scan in Figure 8(b) reveals that, for a partially transformed grain, the twins (red) span across the martensite bands (blue) with twin tips located on the martensite-austenite boundaries. Thus, for grains fully transformed to martensite, twins will appear to be randomly located within the martensite (e.g. the bottom-left grain of Figure 6(b)). To analyze propensity for twinning with respect to the extent of martensite transformation in each grain, Figure 8(c) quantifies the relation of twinning to the percent martensite transformation in the corresponding grains (excluding the edge grains). Filled red circles denote the martensite fraction in the six twinned grains, and red arrows point to the corresponding grains at 55 hours of H charging. Twins appear to only form in grains that have experienced greater than 50% martensite transformation, although there is not an apparent correlation of twinning to the martensite fraction at 55 hours of H charging.

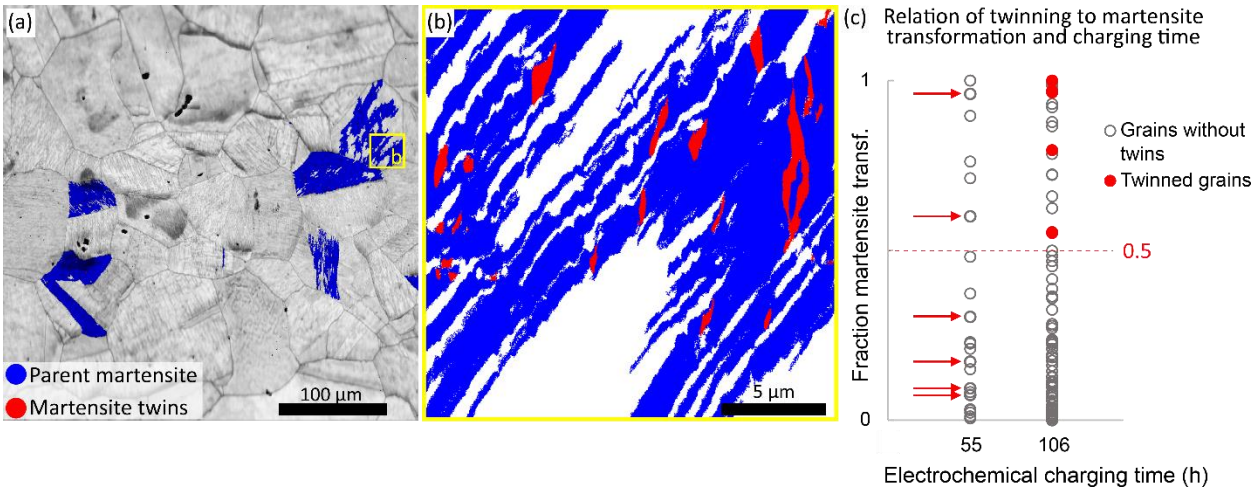

Figure 8. (a) IQ map of a sample H charged for 106 hours. Martensite that contains twins ("parent martensite") is highlighted in blue, and twins that were identified by EBSD scan are in red (those identified within a step size of 0.35 µm). (b) High-resolution EBSD scan of the twinned regions, with martensite in blue, twins in red, and austenite in white. (c) Fraction of fcc→hcp transformation plotted for all non-edge grains in the 400 µm region shown in (a), based on the EBSD phase maps at 0, 55, and 106 hours shown in Figure 2. The 6 twinned grains are represented by red points; these points correspond to ones marked with red arrows at 55 hours.

3.2. Discussion

Figure 9 presents an overview of the observed H-induced transformations in the FeMnCoCr alloy. Beginning from the as-homogenized, mostly austenitic state (10(a)), H induces martensite transformation (10(b)) preferentially in <111> - <101> oriented grains and at Σ3 boundaries. Further increase in H content causes the martensite transformation to progress (10(c)), and H eventually induces $\{10\bar{1}2\}$ type twins within the martensite phase (10(d)). We discuss each of these observations in detail below.

3.2.1 Hydrogen-induced martensite transformation

Increasing H content clearly increases the amount of martensite transformation in this material (as shown by Figure 2), which is in line with the observations of H-induced or H-enhanced martensite

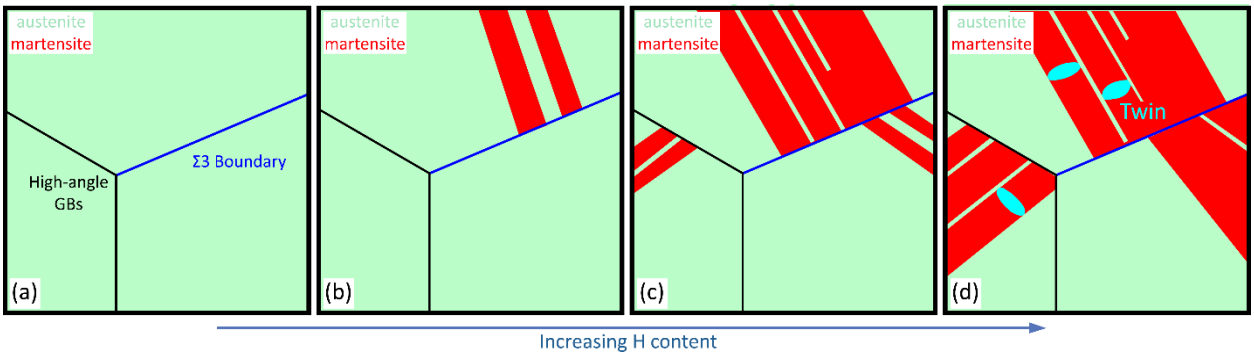

Figure 9. Schematic overview of the H-induced transformations observed in this work. (a) We begin with an austenitic sample, which contains Σ3 boundaries and high-angle GBs. (b) Upon H charging, martensite likely nucleates from a Σ3 boundary. (c) Upon further addition of H, the martensite fraction increases, and (d) twins eventually form at austenite-martensite boundaries.

transformations in stainless steels [119]. The serial sectioning results also indicate that the martensite fraction depends strongly on H content (Figure 3), since the martensite fraction decrease with depth, and since H charging is known to induce a H gradient in the material, with high H concentrations near the surface [120]. We can calculate an approximate critical H concentration for transformation as follows. The TDS results (Figure 1(b)) yield a total hydrogen content of 13.26 wt. ppm, which is the mean concentration throughout the sample thickness (482 μm). However, the value of interest corresponds to the H concentration at 12 μm below the surface (Figure 3(d)). After 106 hours of H-charging time (t), the center of the specimen is expected to be free of H, as the effective H penetration depth is calculated to be about 40 μm (i.e. $x \sim \sqrt{Dt}$, where D is taken to be 1 x 10^{-15} $m^2 s^{-1}$, a typical value for fcc HEAs [121,122]). Here, we consider the hydrogen diffusion process from surface to bulk, where the concentration as a function of the distance below the surface (x) is given by:

$$c(x,t) = c_0\left[1 - \mathrm{erf}\left(\frac{x}{2\sqrt{D \cdot t}}\right)\right] \quad (1)$$

In Equation (1), H charging time, c_0 is H concentration at the surface, and D is the approximate diffusion coefficient at room temperature. The mean atomic fraction in the sample c_M across the sample thickness (i.e. H concentration measured from the TDS method) is given by:

$$c_M = \frac{\int_0^w c(x,t)\,dx}{w} \quad (2)$$

In Equation (2), we take *w* to be half the sample thickness, to account for the fact that the sample is being H charged from both sides at once. By simplifying the above equation, one can rewrite and calculate for the H concentration at surface c_0 with the following equation:

$$c_0 = \frac{w \cdot c_M}{4}\sqrt{\frac{\pi}{D \cdot t}} \quad (3)$$

From Equation (3), c_0 = 36 wt. ppm was obtained. Therefore, from Equation (1), a critical concentration of 24 ± 1 wt. ppm was found for H-induced martensite formation. The calculated error arises from slight variation in applied current during H charging.

The correlation between grain orientation and martensite transformation (Figure 4) further validates the importance of H content to transformation capability. In a previous work, Li *et. al.* used H permeation tests to study the rate of H diffusion in pure Ni single crystals and determined that H diffusion is fastest in grains with a <111> or <101> orientation, with respect to the net diffusion direction in the crystal [110]. Thus, considering that H diffuses into our sample from the surface during H charging, the <111> and <101> grains would take up H faster than other grains and therefore have the highest H content, which results in a relatively larger amount of martensite transformation compared to <100> type grains.

However, these observations regarding H diffusion rate do not explain why some <111> and <101> type grains do not experience martensite transformation within 55 hours of H charging, as represented by the blue grains/points in Figure 4(a-b). It is worth noting that, even if all of these grains have a high enough H content for martensite transformation to occur, it is possible that martensite may not nucleate in every grain, simply due to the nature of nucleation statistics. Here, we also consider other microstructural effects which could contribute to the suppression of martensite. First, we note in Figure

4(c) that, overall, the average grain misorientation for grains within 10 degrees of the <111>-<101> edge of the IPF tends to be lower for martensite-forming grains than the other grains. One interpretation of this observation could take into account the relationship of misorientation to GND density. Generally, higher grain misorientation correlates to a higher GND density [123]; this suggests that the martensite-forming grains begin with a lower GND defect density than the other grains. Meanwhile, it has been shown that H can become trapped at dislocations upon entering the material [7,111]. Thus, one may suppose that the higher GND density could provide a distribution of H traps within a grain such that H may be less likely to reach a critical value near a preferential martensite nucleation location (e.g. at a grain boundary). The second microstructural feature we consider is grain size. For martensite-forming grains, we observe that the diameter is on average higher, compared to the diameters of grains that do not form martensite (Figure 4(c)). Relatedly, it has been reported for Fe-based alloys that the fcc phase can be stabilized against martensite via grain refinement on the order of tens of microns [112,124]. Thus, grains with smaller diameters may exhibit a lower propensity for martensite transformation, although the factor of lower probability of martensite nucleation sites in small grains may also be taken into account here. Overall, while just one of these factors—H diffusion rate, defect density, and grain size—alone may not fully explain martensite transformation within a given grain, some combination of these and other microstructural factors will most likely affect the progression of martensite transformation.

We next consider how H may drive the martensite transformation upon entering the material. As noted earlier, H has been shown to decrease SFE in stainless steels [76] and FeMnCoCrNi [125]. Thus, adding H to the material aids martensite transformation at the stage of nucleation, due to the reduction in free energy of hcp embryos (as related to SFE) [126] and the corresponding nucleation of dislocations necessary for transformation [125]. Because interstitial H could also contribute to local stress fields affecting this transformation, we wish to further consider how interstitial H may relate to transformation dislocation motion. The austenite to ε-martensite transformation requires glide of fcc a/6<$11\bar{2}$> type

partial dislocations on alternating planes to form the hcp phase [126]. This glide could result from the introduction of H [127,128]: our previous calculations revealed that when H segregates to GBs in an fcc material, it can produce a stress field sufficient to drive movement of dislocations within the grains [128]. Thus, we propose that, by segregating to GBs in the FeMnCoCr material, H similarly induces the shear stress and resulting dislocation motion that are necessary for the H-induced martensite transformation. The TDS results validate that H indeed segregates to grain boundaries, including high-angle grain boundaries as indicated by the first peak in Figure 1(b), and Σ3 boundaries, as indicated by the third peak [117,129].

Next, we proceed one step further in explaining the tendency of H-induced martensite to border Σ3 boundaries (Figure 5). According to the Olson-Cohen model, martensite nucleation occurs by faulting from defects such as GBs, where the necessary Shockley partial dislocations are available (often due to dislocation interactions at dislocation pile-ups) [115,116,130]. High-angle GBs in particular have been confirmed to be preferred nucleation sites under stress by Landau modeling of martensite nucleation [131]. Further, boundaries that specifically contain the necessary dislocations within their structure are especially probable nucleation sites, such as noncoherent twin boundaries, whose incoherent segments contain a/6<$11\bar{2}$> partials [115]. The potential of these nucleation sites have also been confirmed experimentally with TEM [132]. Based on the statistical analysis of martensite-austenite boundaries in Figure 5, it appears that the martensite preferentially nucleates on the Σ3 boundaries, instead of nucleating randomly on various GBs. Several instances of small martensite zones growing from only one boundary, such as those shown in Figure 5(b), support the possibility of Σ3 boundaries as nucleation sites. However, the Σ3 boundaries in this material, which are annealing twin boundaries, are expected to be coherent, similar to the case of high-Mn steels [18]. (These fcc annealing twin boundaries should not be confused with the aforementioned hcp twins, which we will discuss in the next section). This gives rise to two problems. First, while coherent Σ3 boundaries have been shown to be slightly more favorable for

nucleation in a single crystal, other GBs are still more favorable nucleation sites in a polycrystalline sample [133], likely due to the lack of intrinsic GB dislocations for Σ3 boundaries [134]. Second, H is expected to not segregate to Σ3 boundaries, due to the increase in the solution energy compared to the bulk octahedral interstitial sites where H may otherwise reside [113,114]; but, based on the TDS curve presented in Figure 1(b), Σ3 boundaries do act as H trap sites.

Koyama *et. al.* thoroughly address the second problem in their work on an Fe-18Mn-1.2C TWIP steel, whose Σ3 deformation twin boundaries were found to contain H via TDA and SKPFM measurements [18,117]. The authors conclude that Σ3 twin boundaries can lose coherency through dislocation-twin interactions, such as the following dislocation dissociation mechanism given by Mahajan *et. al.* [135]:

$$\frac{1}{2}[\bar{1}01]_{(111)} \rightarrow \frac{1}{6}[\bar{1}14]_{(\overline{5}\overline{1}\overline{1})||(111)} + \frac{1}{6}[\overline{211}]_{(\bar{1}11)} \quad (4)$$

Equation (4) shows the specific example of a $[\bar{1}01]$dislocation interacting with a (111) coherent twin. Such dislocation-twin interactions result in incoherent steps on the Σ3 boundaries, which could accommodate interstitial H [117]. Additionally, as a result of the dissociation, the now-incoherent boundary will contain an a/6<$11\bar{2}$> partial dislocation, as shown by the last part of Equation 4. Thus, we reason that H-induced dislocation interactions with Σ3 boundaries simultaneously form incoherent regions to which H can segregate, and, through this process, the incoherent regions of the Σ3 boundaries become viable martensite nucleation sites. Even though there is less H stored at these boundaries compared to high-angle GBs (suggested by TDS results in Figure 1), these nucleation sites, with Shockley partial dislocations readily available, would be statistically more highly probable nucleation sites than random high-angle GBs. This would explain why the martensite is observed to prefer Σ3 boundaries over other GBs.

It remains unclear whether the H first segregates to high-angle grain boundaries, inducing dislocation motion that results in dislocation-Σ3 boundary interactions and further H segregation, or whether there could be small pre-existing incoherent portions of Σ3 boundaries that accept H interstitials

from the beginning. Further investigation is needed to clarify these questions. Either way, our results show that H does segregate to Σ3 boundaries in the FeMnCoCr alloy, which seems to correlate to a preference for martensite nucleation at these boundaries.

3.2.2 Hydrogen-induced twinning in the martensite phase

We now examine the mechanism of twinning within the H-induced martensite. The field of hcp twinning mechanisms is rich and highly debated [118,136–140]. Generally, $\{10\bar{1}2\}[10\bar{1}\bar{1}]$ twins form by a combination of shear (movement of hcp partial dislocations) and atomic shuffling, as shear alone will not produce the full crystallographic transformation from the parent structure to the twin [118]. The end result for the $\{10\bar{1}2\}$ twins is to reach an 86° rotation about the $< 1\bar{2}10 >$ axis with respect to the parent material (as illustrated in Figure 6). This is the main identifying factor we employed to verify the twins' character over a range of grains.

Based on the literature detailing twin formation mechanisms, the relation of stress state to twin type can be deduced from the c/a ratio in an hcp material [140]. The c/a ratio for our FeMnCoCr alloy is 1.6238 [54], and is not expected to significantly change due to H entering the lattice [141]. For this ratio, the twinning shear necessary for $\{10\bar{1}2\} < 10\bar{1}1 >$ twin formation causes extension along the c direction [118,140]. Hence, these twins are referred to as "extension twins." From a mechanical perspective, these extension twins observed after 106 hours of H charging thus form as a result of tension in the hcp phase, parallel to the c axis. This tension might arise from two factors: first, the H-induced stress that causes the martensite transformation in the first place; and, second, H-induced lattice expansion. The latter has been reported to occur in various materials [142–144], including up to 5% expansion in hcp-martensite in stainless steels [141]. While the first option is certainly feasible in terms of inducing c-direction tensile stresses, the H-induced stress from GB segregation should also be compressive in some grains. However, for this c/a ratio, and other hcp materials with c/a greater than 1.5, contraction along the c-axis would be

expected to result in $\{10\bar{1}1\}$ compression twins [118,140]; neither these twins, nor any other common hcp twin variants, were found in the material, including the second, pre-strained sample mentioned in the Results section. Thus, it seems unlikely that this form of H-induced stress is the main driving force for the twin formation; rather, interstitial H within the lattice would be responsible.

Our results further support this hypothesis. It is clear from Figure 8(c) that twinning occurs as a result of high H content. Even after 55 hours of H charging, some grains fully transformed to martensite, indicating that H-induced stresses were already prevalent. However, twinning did not occur in these grains: while it was necessary for grains to have a high martensite content (e.g., over 50%) for twinning to occur, a high martensite content alone was not sufficient. Instead, twinning only occurred after longer H charging times, which produced a high concentration of H on the surface of approximately 36 wt. ppm (assuming homogenous distribution within the sample surface). This H content would have produced significant lattice expansion near the surface, where twins formed. Additionally, by analyzing an EBSD scan of the second, pre-strained sample after letting the H desorb for 3 months at ambient conditions, we found that the H-induced twinning is reversible: most of the twins fully disappeared, leaving behind grains with the exact crystallographic orientation that they had before H charging. Thus, when the H-induced lattice stress was alleviated, the twins reverted in a non-plastic manner, in contrast to the martensite itself, which did not revert upon desorption.

Other effects promoting or limiting twin formation should be noted. Based on the SEM-TDS and serial sectioning analysis, twins only formed at a critical H content of 31 ± 1 wt. ppm, i.e., the content present within 5 μm of the sample surface. Twins generally nucleated at the surface of the sample and decreased in size below the surface. These results indicate that twins were only able to form near the maximum H content; however, additional surface effects may have further increased the twinnability near the surface. First, in a study of nano-sized single crystals, Gong *et. al.* found that, in the presence of free surfaces, coherency stresses associated with twin formation would be partitioned to the matrix [145]. This

observation indicates that the energy barrier for twin formation near surfaces would be lower, compared to the bulk. Second, the surface may serve as a source for partial dislocations necessary for nucleation, as well as twinning dislocations associated with growth [146]. We confirmed the importance of defect density to twin formation with the sample that was pre-strained by 15%: although this sample had a lower H content, it had a much higher twin density, by a factor of 50. Thus, the availability of defects is at least as important to twinnability as H content.

To the best of our knowledge of the literature, this is the first conclusive observation of H-induced twinning in martensite. Previously, H-induced twinning has been observed in fcc single crystals [147,148], ferritic stainless steels [71,149–151] and austenitic equiatomic FeMnCoCr [46]. H has also been shown to enhance deformation twinning in stainless steels due to the decrease in SFE [152], and one instance of H-enhanced deformation twinning in α'-martensite was reported in a high-strength bearing steel [153]. Thus, there is a precedent for H-induced or -enhanced twinning in stainless steels and related alloys. Meanwhile, this instance of H-induced twinning in ε-martensite is unique, and deserves further study due to the potential for increased ductility in the otherwise relatively brittle phase.

3.2.3 Summary

To summarize this chapter, we have now observed a variety of H interactions with microstructure and metastability in this FeMnCoCr alloy. Upon introduction of H into the material, with no externally applied load, the H can induce both martensite transformation and twinning within the martensite, each with complex dependence on H content and microstructure. We would next like to explore how such H-induced transformations may broadly benefit alloys within the FeMnCoCr system. To begin to connect this study to other compositions, we propose to systematically search for H effects on austenite stability and embrittlement over a range of compositions and microstructures. To do so, we could consider a classical HT characterization study, as discussed in section 1.4. However, even simple data (e.g. checking

for indentation-induced cracking) may not be straightforward to compare: due to the combination of metastability, H-induced transformations, transformation dependence on H concentration, and H concentration dependence on microstructure, on top of the compositional complexity, a large amount of data analysis would likely be required in order to draw strong conclusions. Thus, we seek to adjust the classical HT approach by adding an additional step in which we use CALPHAD software to select just a few compositions that will allow us to systematically examine H effects with respect to austenite stability. We perform the first iteration of this study and present the results in the next chapter.

4. High-throughput screening of FeMnCoCr alloys

4.1. Results

We used three criteria for selecting the $Fe_{88-x-y}Mn_{12}Co_xCr_y$ alloys for this study. First, we required that a single fcc phase exist at high temperature, as predicted by equilibrium phase diagrams produced in Thermo-Calc, to enable some fraction of retained austenite upon quenching. We observed that this single fcc phase was always present for the alloys of interest, with Co and Cr contents varying between 5 and 15 at%, and that the fcc phase was predicted to be thermally stabilized at lower temperatures by Mn and Cr, but destabilized by Co. Second, we chose alloys with low free energy of γ-austenite to ε-martensite transformation, $\Delta G^{\gamma\rightarrow\varepsilon}$**,** to enable the TRIP effect [154]; here, Co and Mn were both observed to increase $\Delta G^{\gamma\rightarrow\varepsilon}$ (they stabilized the fcc phase), while Cr decreased it (stabilized the ε phase). Thus, the Co and Cr content could be balanced to choose $\Delta G^{\gamma\rightarrow\varepsilon}\sim 0$. Finally, we adjusted Cr and Co contents to vary the martensite start temperatures, to further vary starting microstructures. The selected compositions and corresponding parameters are displayed in Table 1. After casting and heat treatment, the compositions were measured by EDS, as presented in Table 2. Some error in Co and Fe contents measured by EDS is expected due to overlapping energy signatures.

	Fe	Mn	Co	Cr	$\Delta G^{\gamma \rightarrow \varepsilon}$	α' M_s	ε M_s
Alloy 1	72	12	10	6	~ 0	174°C	9°C
Alloy 2	61	12	14	13	~ 0	168°C	7°C
Alloy 3	70	12	5	13	< 0	113°C	113°C

Table 1. Target compositions for the three selected $Fe_{88-x-y}Mn_{12}Co_xCr_y$ alloys in at%, and the corresponding phase transformation energy and martensite temperatures, as predicted by Thermo-Calc.

	Fe	Mn	Co	Cr
Alloy 1	70.0 ± 1.7	11.5 ± 0.3	11.9 ± 0.4	6.6 ± 0.2
Alloy 2	59.5 ± 1.5	11.9 ± 0.3	14.7 ± 0.5	13.9 ± 0.4
Alloy 3	67.5 ± 1.7	11.8 ± 0.3	6.7 ± 0.3	14.0 ± 0.4

Table 2. Compositions of homogenized alloys measured by EDS in at%.

Samples from these alloys were subjected to three recrystallization treatments at 900°C, for 5, 15, and 30 minutes (referred to as treatment A, B, and C, respectively). After heat treatment and sample preparation, the microstructures of each of the 9 material states (3 compositions x 3 heat treatments) were imaged with BSE in the SEM. Phase fractions were quantified by XRD. These results are summarized below in Figure 10. All microstructures contained a measurable fraction of α' and ε-martensite, while only alloys 2 and 3 exhibited retained γ-austenite. A fine EBSD scan verified that no interlath austenite was detectable in alloy 1 at this time, although further investigation is needed to certify this.

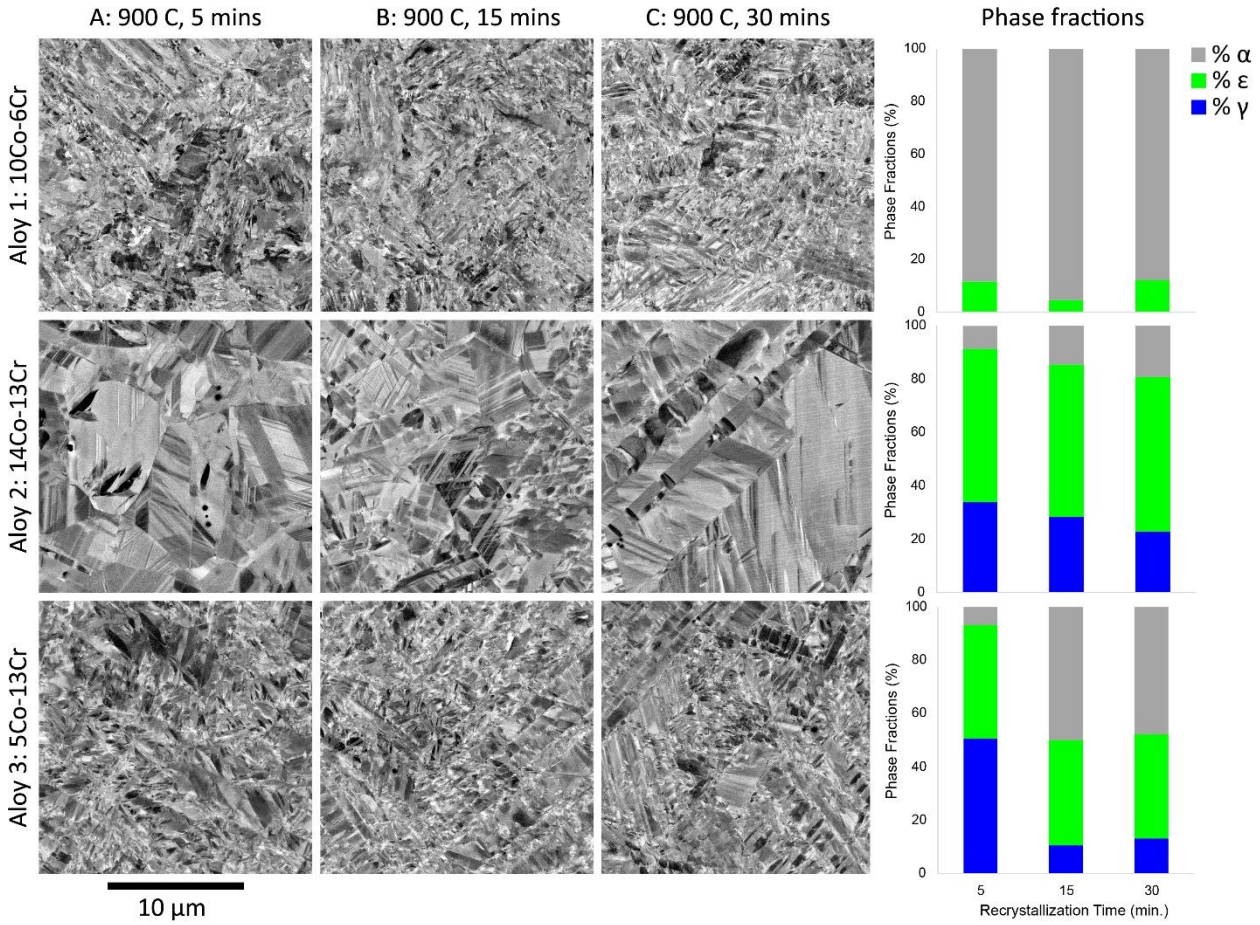

Figure 10. Array of microstructures produced by varying composition and recrystallization treatment durations. Phase fractions for each alloy and recrystallization time are summarized in bar graphs on the right.

The hardness of each sample was measured by Vickers micro-indentation testing after polishing; the average hardness from each set of 5 indents is plotted against α' martensite phase fraction in Figure 11. As a general trend, hardness increased with α' martensite fraction, but trends for individual alloys varied.

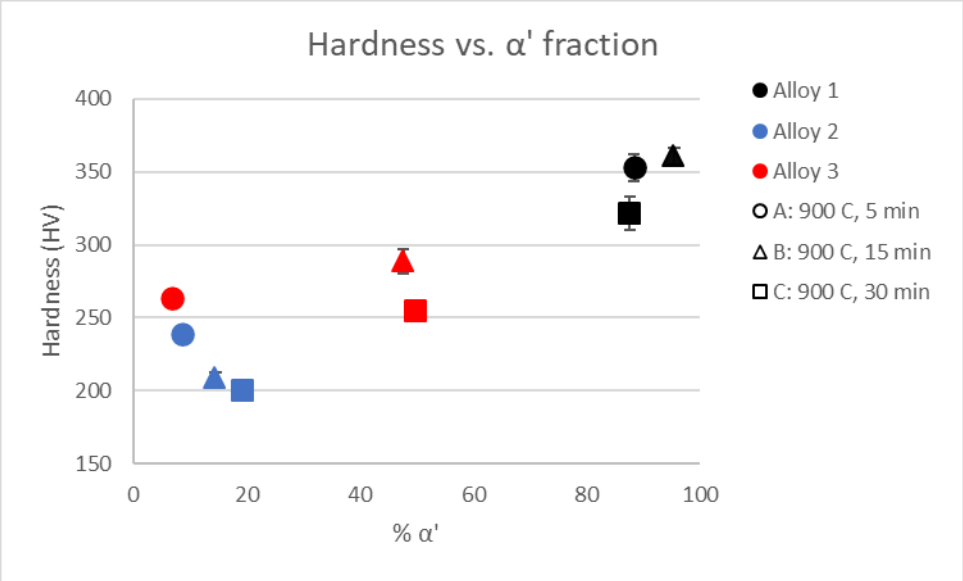

Figure 11. Average hardness measured by Vickers micro-indentation for the 9 material states, in the absence of hydrogen. Error bars indicate standard deviation of the 5 hardness measurements for each sample.

Four samples with varying compositions and fractions of retained austenite were selected for H charging and further analysis: 2A, 2C, 3A, and 3C. Each of these samples was indented before H charging, immediately after 24 hours of H charging at 2.5 mA/cm^2, and again after samples were left to outgas at ambient conditions for 24 hours. The average hardness at each of these times (0, 24, and 48 hours, respectively) is summarized in Figure 12. Generally, introducing H increased the hardness of each sample, then the hardness decreased to an intermediate value after 24 hours of outgassing, at which point some H would likely have remained in the samples due to the slow H diffusion rate in the fcc phase [155]. It is observed that sample 2A experienced the smallest change in hardness overall.

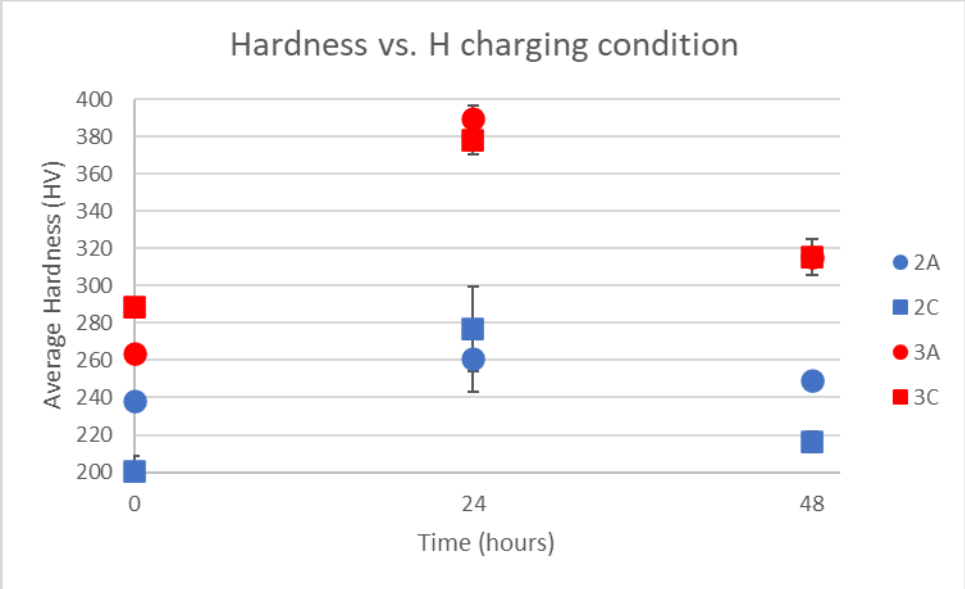

Figure 12. Average hardness measured by Vickers micro-indentation for select samples before H charging (t=0 hours), immediately after 24 hours of H charging at 2.5 mA/cm^2 (t=24 hours), and after outgassing at ambient conditions for 24 further hours (t=48 hours). Error bars represent the standard deviation for each set of measurements.

After each set of indentations, samples were examined with the SEM to determine whether deformation occurred by slip (as determined by the presence of slip steps) and/or mechanically induced α'-martensite transformation, and whether cracking occurred from the indentation. A few instances of α' transformation were verified with EBSD to ensure accurate identification. The indentation response results are summarized in Table 3 below, where "Y" and "N" indicate a positive and negative identification of each feature, respectively. All samples exhibited slip and α' transformation prior to the addition of H ("pre-H") and did not crack initially. These responses varied after introduction of H ("post-H") and after outgassing for 24 hours ("post-outgassing"). For the post-H indentation, indents were performed within 15 minutes of removing the sample from the H charging setup, to minimize H desorption before indenting.

	Pre-H Indentation			Post-H Indentation			Post-Outgassing Indentation		
Sample	Slip?	α' transf?	Cracking?	Slip?	α' transf?	Cracking?	Slip?	α' transf?	Cracking?
2A	Y	Y	N	Y	Y	N	Y	Y	N
2C	Y	Y	N	Y	Y	Y	Y	Y	N
3A	Y	Y	N	Y	N	Y	Y	N	Y
3C	Y	Y	N	Y	N	Y	Y	N	N

Table 3. Indentation response of select alloys before H charging, post H charging, and post outgassing. Slip, α' transformation, and cracking were identified with SEM (both SE and BSE imaging) in each instance. "Y" indicates positive identification of these features, and "N," negative.

4.2. Discussion

Upon selecting compositions for this study, our goal was to produce alloys with varying microstructure and specifically γ-austenite thermal stability. The SEM images and phase fractions displayed in Figure 10 suggest that we were successful on this front. For alloy 1, it appears that the austenite was not stable enough to be retained upon quenching, at least for this set of heat treatments; this observation is supported by the thermodynamic data, as alloy 1 exhibited both the highest α' M_s temperature and lowest Cr content—thus the γ phase was expected to be the least stable. This composition provides an edge case for future studies, where varying Co and Cr content between this alloy and the others could produce interesting microstructures besides those presented here. Alloy 2, in contrast, displayed a more stable γ phase. Accordingly, alloy 2 has a higher Cr content and lower predicted α' M_s temperature than alloy 1. This trend continues for alloy 3, which achieved the highest γ fraction after the 5-minute recrystallization treatment. For alloys 2 and 3, γ fraction could be altered with recrystallization time, and, generally, the γ and α' phase tended to substitute for each other. The relevance of this trade-off for alloy 1, as well as the dependence of ε fraction on the heat treatment parameters, remain open questions that require further investigation.

To examine the relationship between γ stability, introduction of H, and martensite transformation, we next focus on the contrast in indentation response between samples 2A and 3A. Both of these samples exhibited martensite transformation before H charging. Examples of mechanically-induced α' martensite transformation features are displayed in Figure 13(a), where the sharp relief of these features is recognizable with SE imaging. After H charging, the indentation response of sample 2A did not noticeably change: the material still exhibited α' transformation and did not crack. Furthermore, upon H charging, sample 2A exhibited the smallest change in hardness compared to all samples, as shown in Figure 12, indicating that H had the weakest effect on this sample. However, in the presence of H, sample 3A no longer exhibited α' transformation, and cracks formed after indentation (see Figure 13(b)). These results may be justified as follows. In a related work [156], H has been shown to increase the thermodynamic stability of the γ phase, separately from (and simultaneously to) inducing the transformations described in Chapter 3. It appears that the γ phase in sample 2A exhibits a sufficiently low stability such that the addition of H does not inhibit mechanically induced α' transformation. Meanwhile, for sample 3A, the γ stability is higher, to the point that the introduction of H appears to further stabilize the γ phase enough to inhibit α' transformation upon indentation. While the differing microstructures of 2A and 3A will affect the total H content, 2A is expected to have a higher H concentration after charging, due to the larger fraction of α'; thus, this difference further supports the observed variation in γ stability in each sample.

Meanwhile, these preliminary results suggest that the unstable γ phase present in 2A correlates to a tougher, more HE-resistant alloy. While samples 2A and 3A were subjected to the same H charging conditions, and 2A is even expected to contain more H after charging, sample 3A exhibited cracking, while 2A did not. Meanwhile, sample 3A exhibited a more stable γ phase that did not undergo α' transformation after indenting, in contrast to 2A. Thus, we discover an extreme difference in mechanical response

between these two alloys, which alludes to increased toughness correlating to the metastable γ to α' transformation.

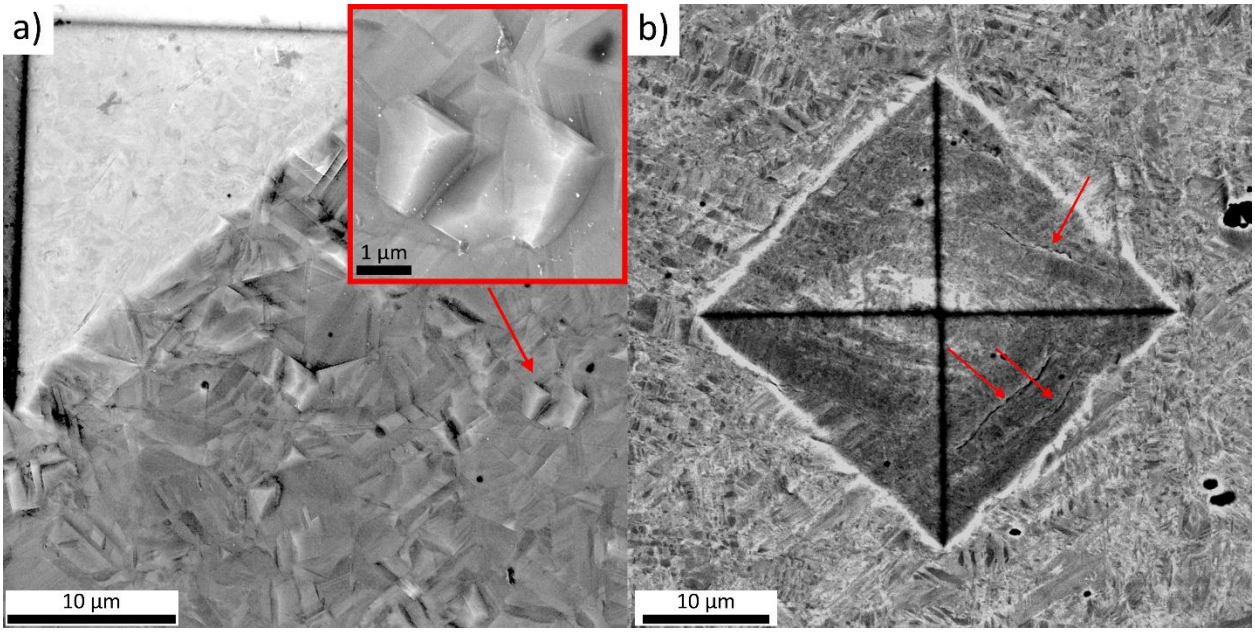

Figure 13. a. SEM SE image of indentation response for sample 2A, before H charging. The inset enlarges an example of indentation induced α'-martensite transformation. b. SEM BSE image of an indent in sample 3A after H charging that exhibits cracking, as indicated with the red arrows.

Although these are only initial results from the first iteration of our screening approach, this iteration has revealed an interesting set of compositions where we find differences in both γ stability and mechanical response. The next step in this high-throughput screening would be to produce other alloys systematically about the compositions of alloys 2 and 3 to discover further trends. Furthermore, the results in Figure 10 show that thermo-mechanical treatments have a strong effect on microstructure and phase constitution, which supplies another interesting degree of freedom for iteration. Thus, these alloys may serve as an interesting starting point to continue exploring this question of metastability-induced toughening, whereby we may further investigate martensite transformations and HE effects in the FeMnCoCrH system.

5. Conclusion

In this work, we first investigated the H-induced microstructural transformations in a metastable $Fe_{45}Mn_{35}Co_{10}Cr_{10}$ HEA. After introducing H via electrochemical charging, we examined the nature of the transformations at the surface of the samples using EBSD, and combined TDS and SEM analyses to quantify the extent of these transformations below the surface. We further quantified the relationship of the transformations to microstructure, including grain orientation and grain boundary type. The main conclusions from this study are listed as follows:

- Upon introduction of H into the $Fe_{45}Mn_{35}Co_{10}Cr_{10}$ specimens, we found that a γ-austenite to ε-martensite transformation took place at the surface of the sample, as shown by EBSD phase mapping. For a sample H charged at 4 mA/cm^2, the martensite extended into the bulk of the sample by about 12 µm from the surface. Based on combined TDS and serial sectioning, this depth corresponded to a critical H concentration of 24 wt. ppm.
- Martensite formed first in grains with faster diffusion rates, as shown by phase and orientation information in the EBSD scans. This observation serves as an additional indication that martensite formation depends strongly on local H content.
- TDS analysis showed that fcc Σ3 annealing twin boundaries served as H traps, and these boundaries were important to martensite formation, as quantified with the EBSD scans. Overall, martensite preferred these boundaries over high-angle grain boundaries, and there were several instances of small martensite grains adjacent to only one Σ3 boundary; this indicates that martensite likely nucleates at Σ3 boundaries. Based on literature, we deduced that this phenomenon probably results from some combination of H trapping at Σ3 boundaries and increased likelihood of partial dislocation emission at these boundaries.

- At longer H charging times, $\{10\bar{1}2\}$ extension twinning occurred near the surface of the ε-martensite at an approximate critical concentration of 31 wt. ppm. These twins form as a result of tension in the hcp lattice, which would be caused by H-induced lattice expansion. To the best of our knowledge, H-induced extension twinning in martensite has not been published elsewhere; further work is required to understand the exact formation mechanisms and possible mechanical benefits of this twinning.

Due to the complexity of these H effects on metastability, in addition to the compositional complexity of the FeMnCoCr system of interest, we next developed a high-throughput method to screen for metastability and H effects in FeMnCoCr alloys. We began by using Thermo-Calc to select three alloys that were expected to yield varying phase constitutions and stabilities due to varying predicted M_s temperatures and energies of ε-martensite transformation. After production and processing of these alloys, we scanned them for hardness, metastable phase transformations, and indentation-induced cracking. Our analysis yielded the following conclusions:

- As a proof-of-principal, we successfully obtained a range of austenite stability and microstructures by a combination of Thermo-Calc predictions and varying thermal treatments. We produced 9 samples (3 compositions x 3 heat treatments) with varying relative amounts of γ, ε, and α' phases, as verified with XRD scans.
- H had varying effects on these alloys, which can be correlated to differing austenite stability and resulting mechanical response, as measured by indentation followed by SEM imaging.
- By focusing on two samples, we found indications that a metastable γ phase is more resistant to HE than a more stable γ phase, which also correlated to the propensity for indentation-induced γ to α' transformation.

- We proposed that these alloys serve as starting compositions about which further iterations of this screening approach may be performed, in order to continue exploring HE and metastability relationships.

6. Outlook

This work leaves us with many opportunities for further research regarding H effects in metastable FeMnCoCr alloys and beyond. Not only do we better understand the many complex interactions H can have with microstructure and transformations in FeMnCoCr, but the high-throughput screening method offers a way to efficiently relate these effects to mechanical properties while also exploring new compositions. Suggestions for further work in these areas are presented below, beginning with the most specific aspects, and ending broadly.

Regarding the H-induced transformations in $Fe_{45}Mn_{35}Co_{10}Cr_{10}$, two directions for improved understanding of the evolution of H and its relation to transformation are as follows. First, while we analyzed microstructure evolution with H charging time (and H content), this work would benefit from a study of the *evolution of H* within the material with respect to time/content. Specifically, a series of TDS measurements after varying H charging times could reveal which H traps become populated with time, and how the H concentrations at these traps changes. After correlating to martensite content, such measurements could also illuminate the most likely martensite nucleation mechanisms, e.g., whether martensite first nucleates at surfaces, high angle grain boundaries, or Σ3 boundaries. Second, regarding twinning at higher H contents, there are several factors to explore in relating H contributions to twinning. While we surmised that twinning occurred as a result of H-induced lattice expansion, further confirmation could be obtained by measuring the lattice parameter with XRD after H charging. This measurement could be compared to known twinning mechanisms to better understand how this lattice expansion relates to

twin formation, and whether there are any other factors at play. Furthermore, a similar microstructural correlation can be carried out for twinning as was done for the H-induced martensite, upon producing a series of samples with higher twin density by increasing the H charging current density. Thus, we could explore in greater depth this unique phenomenon of H-induced hcp twinning.

More generally, these mechanistic H-induced transformation findings could next be connected to mechanical testing of the material (with and without H) to understand the benefits or detriments of these transformations. Often, tensile tests are used to examine the reduction in ductility upon H charging, and these could be applied to this problem. It would be especially interesting to relate cracking behavior to microstructure, which could be done by analysis of surface cracking (for example, Ref. [117]). In particular, preliminary analysis showed that the H-induced martensite in our study was not the main cause of cracking, which is promising for HE resistance. (Similar conclusions were drawn for 304L stainless steel, where atomic H was the cause of cracking [17].) First, we found that a higher relative percent of Σ3 boundaries bordered martensite compared to grain boundaries. In a separate experiment, where a sample was charged for 106 hours with a harsher current density, then allowed to degas for 3 days before taking images with the SEM, we found that cracking was more common on grain boundaries than Σ3 boundaries, despite their correlation to martensite. Although this could be a result of the higher cohesive energy of Σ3 boundaries, this seems unlikely, as H at the boundaries would reduce cohesion. Additionally, in their experiments involving tensile tests of Fe-Mn-C, Koyama *et. al.* found that Σ3 boundaries in the presence of H were highly probable crack propagation sites [117]. Thus, the apparent lack of cracking along Σ3 boundaries in $Fe_{45}Mn_{35}Co_{10}Cr_{10}$ suggests that the martensite at these boundaries either did not contribute to cracking or possibly inhibited cracking; these observations require further investigation to draw stronger conclusions.

The contributions of martensite transformation to toughening in H environments can also be analyzed with the high-throughput screening methods. In particular, we can investigate (1) the

composition/γ metastability dependence of the presence of ε and α' martensites, as well as their associated mechanical transformations, and (2) their relation to HE. The motivation for the case study on $Fe_{45}Mn_{35}Co_{10}Cr_{10}$ included the notion that α' martensite is always detrimental for HE, but the results from our first screening indicate that we should ask ourselves whether this is also true in FeMnCoCr HEAs. A first test could be simply to check for delayed cracking in α' martensite samples compared to others, but mechanical behavior can also be further investigated on a small scale with indentation or a larger scale with tensile testing. Furthermore, it remains unclear exactly when ε martensite may provide toughening (even if this is a rare or common event), with respect to composition and microstructure. Information in these directions could be crucial for designing metastable HE resistant alloys.

Finally, as mentioned at the end of Chapter 4, the alloys explored here could be used as starting compositions for further screening of metastability and HE effects. While we found that Thermo-Calc was a useful tool in producing a range of microstructures and austenite stability, the predictions were limited to relative properties; for example, it remains undetermined what exact compositions will or will not retain austenite, and what factors affect ε martensite fraction. Thus, further iterations about these initial compositions could reveal much more regarding thermo-mechanical treatment response and phase constitution-composition dependence, in addition to mechanical response in H environments. This is an exciting opportunity to investigate H and metastability relationships systematically, which could lead to the design of new HE-resistant alloys.

Acknowledgments

First, I wish to sincerely thank Dr. Cem Tasan, the research advisor for this project, who has dedicated his time to discussion and guidance, on the research itself and beyond.

I would also like to express my great appreciation for my colleagues: Haoxue Yan, with whom I worked closely on untangling the complexities arising from hydrogen—she taught me several experimental methods, provided guidance on data interpretation, and is responsible for the thermal desorption spectroscopy results cited in this work; Dr. Jinwoo Kim, who acted as a second advisor when developing methods for exploring hydrogen effects, and was always willing to offer advice; Shaolou Wei, who had a suggestion for any issue, ranging from polishing techniques to dislocation mechanisms; and Timothy Fountain, for endless advice while we worked on related projects, as well as helping me collect XRD data on short notice.

Furthermore, I owe thanks to Dr. Onur Guvenc, Dr. Hyunseok Oh, Mike Tarkanian, and Dr. Shaymus Hudson who taught me a range of metallurgical techniques and readily offered guidance. And finally, an immense thank-you to the whole Tasan Group: every single member offered me advice or feedback on multiple occasions, and I owe much of the success of this work to their combined support.

References

[1] S. Lynch, Hydrogen embrittlement phenomena and mechanisms, Corros. Rev. 30 (2012) 105–123. https://doi.org/10.1515/corrrev-2012-0502.

[2] M. Koyama, M. Rohwerder, C.C. Tasan, A. Bashir, E. Akiyama, K. Takai, D. Raabe, K. Tsuzaki, Recent progress in microstructural hydrogen mapping in steels: quantification, kinetic analysis, and multi-scale characterisation, Mater. Sci. Technol. (United Kingdom). 33 (2017) 1481–1496. https://doi.org/10.1080/02670836.2017.1299276.

[3] M. Nagumo, Fundamentals of Hydrogen Embrittlement, Springer Singapore, Singapore, 2016. https://doi.org/10.1007/978-981-10-0161-1.

[4] H.K. Birnbaum, P. Sofronis, Hydrogen-enhanced localized plasticity-a mechanism for hydrogen-related fracture, Mater. Sci. Eng. A. (1994). https://doi.org/10.1016/0921-5093(94)90975-X.

[5] I.M. Robertson, H.K. Birnbaum, An HVEM study of hydrogen effects on the deformation and fracture of nickel, Acta Metall. 34 (1986) 353–366. https://doi.org/10.1016/0001-6160(86)90071-4.

[6] J. Von Pezold, L. Lymperakis, J. Neugebeauer, Hydrogen-enhanced local plasticity at dilute bulk H concentrations: The role of H-H interactions and the formation of local hydrides, Acta Mater. 59 (2011) 2969–2980. https://doi.org/10.1016/j.actamat.2011.01.037.

[7] R.. Oriani, The diffusion and trapping of hydrogen in steel, Acta Metall. 18 (1970) 147–157. https://doi.org/10.1016/0001-6160(70)90078-7.

[8] J.P. Hirth, Effects of hydrogen on the properties of iron and steel, Metall. Trans. A. 11 (1980) 861–890. https://doi.org/10.1007/BF02654700.

[9] A.R. Troiano, The role of hydrogen and other interstitials in the mechanical behavior of metals, Trans ASM. 52 (1960) 54.

[10] D. Eliezer, E. Tal-Gutelmacher, T. Boellinghaus, HYDROGEN EMBRITTLEMENT IN HYDRIDE-AND NON HYDRIDE-FORMING SYSTEMS-MICROSTRUCTURAL/PHASE CHANGES AND CRACKING MECHANISMS, n.d.

[11] E. Tal-Gutelmacher, D. Eliezer, Hydrogen-Assisted Degradation of Titanium Based Alloys, n.d.

[12] R.S. Vitt, K. Ono, Hydrogen solubility in alpha titanium, Metall. Trans. 2 (1971) 608–609. https://doi.org/10.1007/BF02663358.

[13] V. Perovic, G.C. Weatherly, C.J. Simpson, Hydride precipitation in α/β zirconium alloys, Acta Metall. 31 (1983) 1381–1391. https://doi.org/10.1016/0001-6160(83)90008-1.

[14] N. Narita, C.J. Altstetter, H.K. Birnbaum, Hydrogen-related Phase Transformations in Austenitic Stainless Steels, Metall. Trans. A, Phys. Metall. Mater. Sci. 13 A (1982) 1355–1365. https://doi.org/10.1007/BF02642872.

[15] G.S. Mogilny, S.M. Teus, V.N. Shyvanyuk, V.G. Gavriljuk, Plastic deformation and phase transformations in austenitic steels in the course of hydrogen charging and subsequent mechanical tests, Mater. Sci. Eng. A. 648 (2015) 260–264. https://doi.org/10.1016/j.msea.2015.09.015.

[16] A. Inoue, Y. Hosoya, T. Masumoto, Effect of Hydrogen on Crack Propagation Behavior and Microstructures Around Cracks in Austenitic Stainless Steels., Trans Iron Steel Inst Jpn. 19 (1979) 170–178. https://doi.org/10.2355/isijinternational1966.19.170.

[17] C. Pan, W.Y. Chu, Z.B. Li, D.T. Liang, Y.J. Su, K.W. Gao, L.J. Qiao, Hydrogen embrittlement induced by atomic hydrogen and hydrogen-induced martensites in type 304L stainless steel, Mater. Sci. Eng. A. 351 (2003) 293–298. https://doi.org/10.1016/S0921-5093(02)00856-0.

[18] M. Koyama, E. Akiyama, Y.K. Lee, D. Raabe, K. Tsuzaki, Overview of hydrogen embrittlement in high-Mn steels, Int. J. Hydrogen Energy. 42 (2017) 12706–12723. https://doi.org/10.1016/j.ijhydene.2017.02.214.

[19] M. Frary, C. Schuh, D.C. Dunand, Strain ratchetting of titanium upon reversible alloying with hydrogen, Philos. Mag. A Phys. Condens. Matter, Struct. Defects Mech. Prop. 81 (2001) 197–212. https://doi.org/10.1080/01418610108216628.

[20] M. Koyama, S.M. Taheri-Mousavi, H. Yan, J. Kim, B.C. Cameron, S.S. Moeini-Ardakani, J. Li, C.C. Tasan, Origin of micrometer-scale dislocation motion during hydrogen desorption, Sci. Adv. 6 (2020) eaaz1187. https://doi.org/10.1126/sciadv.aaz1187.

[21] I.M. Robertson, The effect of hydrogen on dislocation dynamics, Eng. Fract. Mech. 68 (2001) 671–692. https://doi.org/10.1016/S0013-7944(01)00011-X.

[22] L. Liu, B. He, M. Huang, The Role of Transformation-Induced Plasticity in the Development of Advanced High Strength Steels, Adv. Eng. Mater. 20 (2018) 1–17. https://doi.org/10.1002/adem.201701083.

[23] M. Soleimani, A. Kalhor, H. Mirzadeh, Transformation-induced plasticity (TRIP) in advanced steels: A review, Mater. Sci. Eng. A. 795 (2020). https://doi.org/10.1016/j.msea.2020.140023.

[24] R.M. McMEEKING, A.G. EVANS, Mechanics of Transformation-Toughening in Brittle Materials, J. Am. Ceram. Soc. (1982). https://doi.org/10.1111/j.1151-2916.1982.tb10426.x.

[25] S.K. Hann, J.D. Gates, A transformation toughening white cast iron, J. Mater. Sci. (1997). https://doi.org/10.1023/A:1018544204267.

[26] S.D. Antolovich, B. Singh, On the toughness increment associated with the austenite to martensite phase transformation in TRIP steels, Metall. Mater. Trans. B. 2 (1971) 2135–2141. https://doi.org/10.1007/BF02917542.

[27] J.H. Ryu, Y.S. Chun, C.S. Lee, H.K.D.H. Bhadeshia, D.W. Suh, Effect of deformation on hydrogen trapping and effusion in TRIP-assisted steel, Acta Mater. 60 (2012) 4085–4092. https://doi.org/10.1016/j.actamat.2012.04.010.

[28] S.D. Pu, A. Turk, S. Lenka, S.W. Ooi, Study of hydrogen release resulting from the transformation of austenite into martensite, Mater. Sci. Eng. A. 754 (2019) 628–635. https://doi.org/10.1016/j.msea.2019.03.098.

[29] M. Koyama, D. Yamasaki, T. Nagashima, C.C. Tasan, K. Tsuzaki, In situ observations of silver-decoration evolution under hydrogen permeation: Effects of grain boundary misorientation on hydrogen flux in pure iron, Scr. Mater. 129 (2017) 48–51. https://doi.org/10.1016/j.scriptamat.2016.10.027.

[30] A. Laureys, T. Depover, R. Petrov, K. Verbeken, Characterization of hydrogen induced cracking in TRIP-assisted steels, in: Int. J. Hydrogen Energy, 2015. https://doi.org/10.1016/j.ijhydene.2015.06.017.

[31] Y.D. Park, I.S. Maroef, A. Landau, D.L. Olson, Retained Austenite as a Hydrogen Trap in Steel Welds, Weld. Res. (2002) 27–35.

[32] K.G. Solheim, J.K. Solberg, J. Walmsley, F. Rosenqvist, T.H. Bjørnå, The role of retained austenite in hydrogen embrittlement of supermartensitic stainless steel, Eng. Fail. Anal. 34 (2013) 140–149. https://doi.org/10.1016/j.engfailanal.2013.07.025.

[33] B.C. Cameron, M. Koyama, C.C. Tasan, Phase Stability Effects on Hydrogen Embrittlement Resistance in Martensite–Reverted Austenite Steels, Metall. Mater. Trans. A Phys. Metall. Mater. Sci. 50 (2019) 29–34. https://doi.org/10.1007/s11661-018-4948-x.

[34] M. Koyama, C.C. Tasan, K. Tsuzaki, Overview of metastability and compositional complexity effects for hydrogen-resistant iron alloys: Inverse austenite stability effects, Eng. Fract. Mech. 214 (2019) 123–133. https://doi.org/10.1016/J.ENGFRACMECH.2019.03.049.

[35] M. Koyama, C.C. Tasan, T. Nagashima, E. Akiyama, D. Raabe, K. Tsuzaki, Hydrogen-assisted damage in austenite/martensite dual-phase steel, Philos. Mag. Lett. 96 (2016) 9–18. https://doi.org/10.1080/09500839.2015.1130275.

[36] M. Koyama, T. Eguchi, K. Ichii, C.C. Tasan, K. Tsuzaki, A new design concept for prevention of hydrogen-induced mechanical degradation: Viewpoints of metastability and high entropy, Procedia Struct. Integr. 13 (2018) 292–297. https://doi.org/10.1016/j.prostr.2018.12.049.

[37] D.B. Miracle, O.N. Senkov, A critical review of high entropy alloys and related concepts, Acta Mater. 122 (2017) 448–511. https://doi.org/10.1016/j.actamat.2016.08.081.

[38] B. Cantor, I.T.H. Chang, P. Knight, A.J.B. Vincent, Microstructural development in equiatomic multicomponent alloys, Mater. Sci. Eng. A. 375–377 (2004) 213–218. https://doi.org/https://doi.org/10.1016/j.msea.2003.10.257.

[39] J.W. Yeh, S.K. Chen, S.J. Lin, J.Y. Gan, T.S. Chin, T.T. Shun, C.H. Tsau, S.Y. Chang, Nanostructured high-entropy alloys with multiple principal elements: Novel alloy design concepts and outcomes, Adv. Eng. Mater. 6 (2004) 299–303. https://doi.org/10.1002/adem.200300567.

[40] T.K. Chen, T.T. Shun, J.W. Yeh, M.S. Wong, Nanostructured nitride films of multi-element high-entropy alloys by reactive DC sputtering, Surf. Coatings Technol. 188–189 (2004) 193–200. https://doi.org/10.1016/j.surfcoat.2004.08.023.

[41] C.Y. Hsu, J.W. Yeh, S.K. Chen, T.T. Shun, Wear resistance and high-temperature compression strength of Fcc CuCoNiCrAl0.5Fe alloy with boron addition, Metall. Mater. Trans. A Phys. Metall. Mater. Sci. 35 A (2004) 1465–1469. https://doi.org/10.1007/s11661-004-0254-x.

[42] P.-K. Huang, J.-W. Yeh, T.-T. Shun, S.-K. Chen, Multi-Principal-Element Alloys with Improved Oxidation and Wear Resistance for Thermal Spray Coating, Adv. Eng. Mater. 6 (2004) 74–78. https://doi.org/10.1002/adem.200300507.

[43] J.W. Yeh, S.K. Chen, J.Y. Gan, S.J. Lin, T.S. Chin, T.T. Shun, C.H. Tsau, S.Y. Chang, Formation of simple crystal structures in Cu-Co-Ni-Cr-Al-Fe-Ti-V alloys with multiprincipal metallic elements, Metall. Mater. Trans. A Phys. Metall. Mater. Sci. 35 A (2004) 2533–2536.

https://doi.org/10.1007/s11661-006-0234-4.

[44] A. Gali, E.P. George, Tensile properties of high- and medium-entropy alloys, Intermetallics. 39 (2013) 74–78. https://doi.org/10.1016/j.intermet.2013.03.018.

[45] F. Otto, A. Dlouhý, C. Somsen, H. Bei, G. Eggeler, E.P. George, The influences of temperature and microstructure on the tensile properties of a CoCrFeMnNi high-entropy alloy, Acta Mater. 61 (2013) 5743–5755. https://doi.org/http://dx.doi.org/10.1016/j.actamat.2013.06.018.

[46] H. Luo, Z. Li, D. Raabe, Hydrogen enhances strength and ductility of an equiatomic high-entropy alloy, Sci. Rep. 7 (2017) 9892. https://doi.org/10.1038/s41598-017-10774-4.

[47] H. Luo, W. Lu, X. Fang, D. Ponge, Z. Li, D. Raabe, Beating hydrogen with its own weapon: Nano-twin gradients enhance embrittlement resistance of a high-entropy alloy, Mater. Today. 21 (2018) 1003–1009. https://doi.org/10.1016/J.MATTOD.2018.07.015.

[48] B. Gludovatz, A. Hohenwarter, K.V.S. Thurston, H. Bei, Z. Wu, E.P. George, R.O. Ritchie, Exceptional damage-tolerance of a medium-entropy alloy CrCoNi at cryogenic temperatures, Nat. Commun. 7 (2016) 1–8. https://doi.org/10.1038/ncomms10602.

[49] Z. Tang, T. Yuan, C.W. Tsai, J.W. Yeh, C.D. Lundin, P.K. Liaw, Fatigue behavior of a wrought Al<inf>0.5</inf>CoCrCuFeNi two-phase high-entropy alloy, Acta Mater. 99 (2015) 247–258. https://doi.org/10.1016/j.actamat.2015.07.004.

[50] J. Chen, X. Zhou, W. Wang, B. Liu, Y. Lv, W. Yang, D. Xu, Y. Liu, A review on fundamental of high entropy alloys with promising high–temperature properties, J. Alloys Compd. 760 (2018) 15–30. https://doi.org/10.1016/j.jallcom.2018.05.067.

[51] Y. Deng, C.C. Tasan, K.G. Pradeep, H. Springer, A. Kostka, D. Raabe, Design of a twinning-induced plasticity high entropy alloy, Acta Mater. 94 (2015) 124–133. https://doi.org/10.1016/j.actamat.2015.04.014.

[52] Z. Li, K.G. Pradeep, Y. Deng, D. Raabe, C.C. Tasan, Metastable high-entropy dual-phase alloys overcome the strength-ductility trade-off, Nature. 534 (2016) 227–230. https://doi.org/10.1038/nature17981.

[53] M. Koyama, C.C. Tasan, K. Tsuzaki, Overview of metastability and compositional complexity effects for hydrogen-resistant iron alloys: Inverse austenite stability effects, Eng. Fract. Mech. 214 (2019) 123–133. https://doi.org/10.1016/j.engfracmech.2019.03.049.

[54] S. Wei, M. Jiang, C.C. Tasan, Interstitial-Free Bake Hardening Realized by Epsilon Martensite Reverse Transformation, Metall. Mater. Trans. A Phys. Metall. Mater. Sci. 50 (2019) 3985–3991. https://doi.org/10.1007/s11661-019-05344-4.

[55] S. Wei, J. Kim, J.L. Cann, R. Gholizadeh, N. Tsuji, C.C. Tasan, Plastic strain-induced sequential martensitic transformation, Scr. Mater. 185 (2020) 36–41. https://doi.org/10.1016/j.scriptamat.2020.03.060.

[56] Z. Li, C.C. Tasan, K.G. Pradeep, D. Raabe, A TRIP-assisted dual-phase high-entropy alloy: Grain size and phase fraction effects on deformation behavior, Acta Mater. 131 (2017) 323–335. https://doi.org/10.1016/j.actamat.2017.03.069.

[57] Q. Yang, L.J. Qiao, S. Chiovelli, J.L. Luo, Critical hydrogen charging conditions for martensite

transformation and surface cracking in type 304 stainless steel, Scr. Mater. 40 (1999) 1209–1214. https://doi.org/10.1016/S1359-6462(99)00093-7.

[58] S. Tähtinen, P. Nenonen, H. Hänninen, Hydrogen-Induced Phase Transformations in Thin Specimens of an Austenitic Stainless Steel, in: Chem. Phys. Fract., Springer Netherlands, 1987: pp. 568–573. https://doi.org/10.1007/978-94-009-3665-2_32.

[59] M.L. Holzworth, M.R. Louthan, Hydrogen-Induced Phase Transformations in Type 304L Stainless Steels, Corrosion. 24 (1968) 110–124. https://doi.org/10.5006/0010-9312-24.4.110.

[60] A. Röhsler, O. Sobol, G. Nolze, W.E.S. Unger, T. Böllinghaus, Use of time-of-flight secondary ion mass spectrometry for the investigation of hydrogen-induced effects in austenitic steel AISI 304L, J. Vac. Sci. Technol. B, Nanotechnol. Microelectron. Mater. Process. Meas. Phenom. 36 (2018) 03F103. https://doi.org/10.1116/1.5013931.

[61] A. Głowacka, M.J. Woźniak, G. Nolze, W.A. Świątnicki, Hydrogen induced phase transformations in austenitic-ferritic steel, in: Solid State Phenom., 2006: pp. 133–140. https://doi.org/10.4028/www.scientific.net/SSP.112.133.

[62] J.M. Rigsbee, TEM observations on hydrogen-induced ϵ-HCP martensite, Metallography. 11 (1978) 493–498. https://doi.org/10.1016/0026-0800(72)90074-2.

[63] S.M. Teus, V.N. Shyvanyuk, V.G. Gavriljuk, Hydrogen-induced γ→ε transformation and the role of ε-martensite in hydrogen embrittlement of austenitic steels, Mater. Sci. Eng. A. 497 (2008) 290–294. https://doi.org/10.1016/j.msea.2008.07.003.

[64] S. Tähtinen, P. Nenonen, H. Hänninen, Hydrogen-induced phase transformations in an austenitic stainless steel, Scr. Metall. 20 (1986) 153–157. https://doi.org/10.1016/0036-9748(86)90231-0.

[65] V.N. Shivanyuk, J. Foct, V.G. Gavriljuk, On a role of hydrogen-induced ε-martensite in embrittlement of stable austenitic steel, Scr. Mater. 49 (2003) 601–606. https://doi.org/10.1016/S1359-6462(03)00338-5.

[66] S. Pu, Hydrogen in Austenite : What Changes after Martensitic Transformation ?, (2018).

[67] M. Koyama, N. Terao, K. Tsuzaki, Revisiting the effects of hydrogen on deformation-induced γ-ε martensitic transformation, Mater. Lett. 249 (2019) 197–200. https://doi.org/10.1016/j.matlet.2019.04.093.

[68] J.A. Venables, The martensite transformation in stainless steel, Philos. Mag. 7 (1962) 35–44. https://doi.org/10.1080/14786436208201856.

[69] Q. Yang, J.L. Luo, Martensite transformation and surface cracking of hydrogen charged and outgassed type 304 stainless steel, Mater. Sci. Eng. A. 288 (2000) 75–83. https://doi.org/10.1016/S0921-5093(00)00833-9.

[70] L. Claeys, T. Depover, I. DeGraeve, K. Verbeken, Electrochemical hydrogen charging of duplex stainless steel, Corrosion. (2018) 2959. https://doi.org/10.5006/2959.

[71] M. Tanino, H. Komatsu, S. Funaki, Hydrogen Induced Martensitic Transformation and Twin Formation in Stainless Steels., in: J. Phys. (Paris), Colloq., EDP Sciences, 1982: pp. C4-503-C4-508. https://doi.org/10.1051/jphyscol:1982478.

[72] A. Röhsler, O. Sobol, W.E.S. Unger, T. Böllinghaus, Comprehensive study of deuterium-induced

effects in austenitic stainless steel AISI 304L, Int. J. Hydrogen Energy. 44 (2019) 12228–12238. https://doi.org/10.1016/j.ijhydene.2019.03.058.

[73] R.P. Frohmberg, W.J. Barnett, A.R. Troiano, Delayed Failure and Hydrogen Embrittlement in Steel, ASM Trans. 47 (1955) 892–925.

[74] M.B. WHITEMAN, A.R. Troiano, The influence of hyrdrogen on the stacking fault energy of an austenitic stainless steel, Phys. Status Solidi. 7 (1964).

[75] A.E. Pontini, J.D. Hermida, X-ray diffraction measurement of the stacking fault energy reduction induced by hydrogen in an AISI 304 steel, Scr. Mater. 37 (1997) 1831–1837. https://doi.org/10.1016/S1359-6462(97)00332-1.

[76] P.J. Ferreira, I.M. Robertson, H.K. Birnbaum, Influence of hydrogen on the stacking-fault energy of an austenitic stainless steel, Mater. Sci. Forum. 207–209 (1996) 93–96. https://doi.org/10.4028/www.scientific.net/msf.207-209.93.

[77] J.D. Hermida, A. Roviglione, Stacking fault energy decrease in austenitic stainless steels induced by hydrogen pairs formation, Scr. Mater. 39 (1998) 1145–1149. https://doi.org/10.1016/S1359-6462(98)00285-1.

[78] M. Koyama, K. Hirata, Y. Abe, A. Mitsuda, S. Iikubo, K. Tsuzaki, An unconventional hydrogen effect that suppresses thermal formation of the hcp phase in fcc steels, Sci. Rep. 8 (2018) 1–8. https://doi.org/10.1038/s41598-018-34542-0.

[79] F.G. Coury, P. Wilson, K.D. Clarke, M.J. Kaufman, A.J. Clarke, High-throughput solid solution strengthening characterization in high entropy alloys, Acta Mater. 167 (2019) 1–11. https://doi.org/10.1016/j.actamat.2019.01.029.

[80] M.A. Melia, S.R. Whetten, R. Puckett, M. Jones, M.J. Heiden, N. Argibay, A.B. Kustas, High-throughput additive manufacturing and characterization of refractory high entropy alloys, Appl. Mater. Today. 19 (2020) 100560. https://doi.org/10.1016/j.apmt.2020.100560.

[81] S.A. Kube, S. Sohn, D. Uhl, A. Datye, A. Mehta, J. Schroers, Phase selection motifs in High Entropy Alloys revealed through combinatorial methods: Large atomic size difference favors BCC over FCC, Acta Mater. 166 (2019) 677–686. https://doi.org/10.1016/j.actamat.2019.01.023.

[82] A. Kauffmann, M. Stüber, H. Leiste, S. Ulrich, S. Schlabach, D.V. Szabó, S. Seils, B. Gorr, H. Chen, H.J. Seifert, M. Heilmaier, Combinatorial exploration of the High Entropy Alloy System Co-Cr-Fe-Mn-Ni, Surf. Coatings Technol. 325 (2017) 174–180. https://doi.org/10.1016/j.surfcoat.2017.06.041.

[83] Y.J. Li, A. Savan, A. Kostka, H.S. Stein, A. Ludwig, Accelerated atomic-scale exploration of phase evolution in compositionally complex materials, Mater. Horizons. 5 (2018) 86–92. https://doi.org/10.1039/c7mh00486a.

[84] S. Thienhaus, D. Naujoks, J. Pfetzing-Micklich, D. König, A. Ludwig, Rapid identification of areas of interest in thin film materials libraries by combining electrical, optical, X-ray diffraction, and mechanical high-throughput measurements: A case study for the system ni-al, ACS Comb. Sci. 16 (2014) 686–694. https://doi.org/10.1021/co5000757.

[85] M.A. Payne, J.B. Miller, M.E. Oliveros, G. Perez, C.P. Gouvea, B.S. Archanjo, C.A. Achete, A.J. Gellman, Assessment of a High-Throughput Methodology for the Study of Alloy Oxidation using

AlxFeyNi1-x-y Composition Gradient Thin Films, ACS Comb. Sci. 18 (2016) 425–436. https://doi.org/10.1021/acscombsci.6b00030.

[86] M. Moorehead, K. Bertsch, M. Niezgoda, C. Parkin, M. Elbakhshwan, K. Sridharan, C. Zhang, D. Thoma, A. Couet, High-throughput synthesis of Mo-Nb-Ta-W high-entropy alloys via additive manufacturing, Mater. Des. 187 (2020) 108358. https://doi.org/10.1016/j.matdes.2019.108358.

[87] C. Haase, F. Tang, M.B. Wilms, A. Weisheit, B. Hallstedt, Combining thermodynamic modeling and 3D printing of elemental powder blends for high-throughput investigation of high-entropy alloys – Towards rapid alloy screening and design, Mater. Sci. Eng. A. 688 (2017) 180–189. https://doi.org/10.1016/j.msea.2017.01.099.

[88] H. Knoll, S. Ocylok, A. Weisheit, H. Springer, E. Jägle, D. Raabe, Combinatorial Alloy Design by Laser Additive Manufacturing, Steel Res. Int. 88 (2017) 1–11. https://doi.org/10.1002/srin.201600416.

[89] M. Cristobal, D. San-Martin, C. Capdevila, J.A. Jiménez, S. Milenkovic, Rapid fabrication and characterization of AISI 304 stainless steels modified with Cu additions by additive alloy melting (ADAM), J. Mater. Res. Technol. 7 (2018) 450–460. https://doi.org/10.1016/j.jmrt.2017.12.001.

[90] Y. Xu, Y. Bu, J. Liu, H. Wang, In-situ high throughput synthesis of high-entropy alloys, Scr. Mater. 160 (2019) 44–47. https://doi.org/10.1016/j.scriptamat.2018.09.040.

[91] Z. Li, A. Ludwig, A. Savan, H. Springer, D. Raabe, Combinatorial metallurgical synthesis and processing of high-entropy alloys, J. Mater. Res. 33 (2018) 3156–3169. https://doi.org/10.1557/jmr.2018.214.

[92] Y. Chen, E. Hintsala, N. Li, B.R. Becker, J.Y. Cheng, B. Nowakowski, J. Weaver, D. Stauffer, N.A. Mara, High-Throughput Nanomechanical Screening of Phase-Specific and Temperature-Dependent Hardness in AlxFeCrNiMn High-Entropy Alloys, Jom. 71 (2019) 3368–3377. https://doi.org/10.1007/s11837-019-03714-2.

[93] N.P. Lavery, S. Mehraban, C. Pleydell-Pearce, S.G.R. Brown, D.J. Jarvis, W. Voice, M. Brunnock, Combinatorial development and high throughput materials characterisation of steels, Ironmak. Steelmak. 42 (2015) 727–733. https://doi.org/10.1179/0301923315Z.000000000419.

[94] S. Parvinian, Y.C. Yabansu, A. Khosravani, H. Garmestani, S.R. Kalidindi, High-Throughput Exploration of the Process Space in 18% Ni (350) Maraging Steels via Spherical Indentation Stress–Strain Protocols and Gaussian Process Models, Integr. Mater. Manuf. Innov. 9 (2020) 199–212. https://doi.org/10.1007/s40192-020-00177-1.

[95] H. Springer, D. Raabe, Rapid alloy prototyping: Compositional and thermo-mechanical high throughput bulk combinatorial design of structural materials based on the example of 30Mn-1.2C-xAl triplex steels, Acta Mater. 60 (2012) 4950–4959. https://doi.org/10.1016/j.actamat.2012.05.017.

[96] H. Springer, M. Belde, D. Raabe, Bulk combinatorial design of ductile martensitic stainless steels through confined martensite-to-austenite reversion, Mater. Sci. Eng. A. 582 (2013) 235–244. https://doi.org/10.1016/j.msea.2013.06.036.

[97] C. Baron, H. Springer, Property-Driven Development of Metallic Structural Materials by Combinatorial Techniques on the Example of Fe–C–Cr Steels, Steel Res. Int. 90 (2019). https://doi.org/10.1002/srin.201900404.

[98] K.G. Pradeep, C.C. Tasan, M.J. Yao, Y. Deng, H. Springer, D. Raabe, Non-equiatomic high entropy alloys: Approach towards rapid alloy screening and property-oriented design, Mater. Sci. Eng. A. 648 (2015) 183–192. https://doi.org/10.1016/j.msea.2015.09.010.

[99] M. Soleimani, A. Kalhor, H. Mirzadeh, Transformation-induced plasticity (TRIP) in advanced steels: A review, Mater. Sci. Eng. A. 795 (2020) 140023. https://doi.org/10.1016/j.msea.2020.140023.

[100] C. Tong, Q. Rong, V.A. Yardley, X. Li, J. Luo, G. Zhu, Z. Shi, New developments and future trends in low-temperature hot stamping technologies: A review, Metals (Basel). 10 (2020) 1–27. https://doi.org/10.3390/met10121652.

[101] A. Turnbull, Perspectives on hydrogen uptake, diffusion and trapping, Int. J. Hydrogen Energy. 40 (2015) 16961–16970. https://doi.org/10.1016/j.ijhydene.2015.06.147.

[102] Y.N. Picard, Scanning Electron Microscopy, in: Mater. Charact., ASM International, 2019: pp. 543–575. https://doi.org/10.31399/asm.hb.v10.a0006668.

[103] W.D. Callister, D.G. Rethwisch, Materials Science and Engineering: An Introduction, 9E ed., John Wiley & Sons, Inc., 2014.

[104] MIT CMSE X-ray Diffraction Facility, (n.d.). http://prism.mit.edu/xray/instruments/gadds.html (accessed April 17, 2021).

[105] K. Takai, G. Yamauchi, M. Nakamura, M. Nagumo, Hydrogen Trapping Characteristics of Cold-Drawn Pure Iron and Eutectoid Steel Evaluated by Thermal Desorption Spectrometry, J. Japan Inst. Met. 62 (1998) 267–275. https://doi.org/10.2320/jinstmet1952.62.3_267.

[106] J.R. Davis, ed., Mechanical Testing, in: Met. Handb. Desk Ed., ASM International, 1998: pp. 1308–1342. https://doi.org/10.31399/asm.hb.mhde2.a0003241.

[107] M. Tiryakioğlu, On the relationship between Vickers hardness and yield stress in Al-Zn-Mg-Cu Alloys, Mater. Sci. Eng. A. 633 (2015) 17–19. https://doi.org/10.1016/j.msea.2015.02.073.

[108] S. Takagi, K. Kamijo, T. Usuda, H. Kawachi, K. Hanaki, Wide-range verification of the geometry of Vickers diamond indenters, 18th IMEKO World Congr. 2006 Metrol. a Sustain. Dev. 1 (2006) 813–817.

[109] Z. Hua, B. An, T. Iijima, C. Gu, J. Zheng, The finding of crystallographic orientation dependence of hydrogen diffusion in austenitic stainless steel by scanning Kelvin probe force microscopy, Scr. Mater. 131 (2017) 47–50. https://doi.org/10.1016/j.scriptamat.2017.01.003.

[110] J. Li, A. Oudriss, A. Metsue, J. Bouhattate, X. Feaugas, Anisotropy of hydrogen diffusion in nickel single crystals: The effects of self-stress and hydrogen concentration on diffusion, Sci. Rep. 7 (2017) 1–9. https://doi.org/10.1038/srep45041.

[111] J. Song, W.A. Curtin, Mechanisms of hydrogen-enhanced localized plasticity: An atomistic study using α-Fe as a model system, Acta Mater. (2014). https://doi.org/10.1016/j.actamat.2014.01.008.

[112] S. Kajiwara, Roles of dislocations and grain boundaries in martensite nucleation, Metall. Mater. Trans. A. 17 (1986) 1693–1702. https://doi.org/10.1007/BF02817268.

[113] Y.A. Du, L. Ismer, J. Rogal, T. Hickel, J. Neugebauer, R. Drautz, First-principles study on the

interaction of H interstitials with grain boundaries in α- and γ-Fe, Phys. Rev. B - Condens. Matter Mater. Phys. 84 (2011) 1–13. https://doi.org/10.1103/PhysRevB.84.144121.

[114] A. Tehranchi, W.A. Curtin, Atomistic study of hydrogen embrittlement of grain boundaries in nickel: I. Fracture, J. Mech. Phys. Solids. 101 (2017) 150–165. https://doi.org/10.1016/j.jmps.2017.01.020.

[115] G.B. Olson, M. Cohen, A general mechanism of martensitic nucleation: Part II. FCC→ BCC and other martensitic transformations, Metall. Trans. A. 7 (1976) 1905–1914.

[116] J.B. Cohen, J. Weertman, A dislocation model for twinning in f.c.c. metals, Acta Metall. 11 (1963) 996–998. https://doi.org/10.1016/0001-6160(63)90033-6.

[117] M. Koyama, A. Bashir, M. Rohwerder, S. V. Merzlikin, E. Akiyama, K. Tsuzaki, D. Raabe, Spatially and Kinetically Resolved Mapping of Hydrogen in a Twinning-Induced Plasticity Steel by Use of Scanning Kelvin Probe Force Microscopy, J. Electrochem. Soc. 162 (2015) C638–C647. https://doi.org/10.1149/2.0131512jes.

[118] Y.F. Guo, S. Xu, X.Z. Tang, Y.S. Wang, S. Yip, Twinnability of hcp metals at the nanoscale, J. Appl. Phys. 115 (2014). https://doi.org/10.1063/1.4881756.

[119] N. Narita, C.J. Altstetter, H.K. Birnbaum, Hydrogen-Related Phase Transformations in Austenitic Stainless Steels., Metall. Trans. A, Phys. Metall. Mater. Sci. 13 A (1982) 1355–1365. https://doi.org/10.1007/BF02642872.

[120] M. Koyama, K. Hirata, Y. Abe, A. Mitsuda, S. Iikubo, K. Tsuzaki, An unconventional hydrogen effect that suppresses thermal formation of the hcp phase in fcc steels, Sci. Rep. 8 (2018) 1–8. https://doi.org/10.1038/s41598-018-34542-0.

[121] D. Ilin, Simulation of hydrogen diffusion in fcc polycrystals. Effect of deformation and grain boundaries : effect of deformation and grain boundaries., Université de Bordeaux, 2014.

[122] K. Hirata, S. Iikubo, M. Koyama, K. Tsuzaki, H. Ohtani, First-Principles Study on Hydrogen Diffusivity in BCC, FCC, and HCP Iron, Metall. Mater. Trans. A Phys. Metall. Mater. Sci. 49 (2018) 5015–5022. https://doi.org/10.1007/s11661-018-4815-9.

[123] W. Pantleon, Resolving the geometrically necessary dislocation content by conventional electron backscattering diffraction, Scr. Mater. 58 (2008) 994–997. https://doi.org/10.1016/j.scriptamat.2008.01.050.

[124] Y. Matsuoka, T. Iwasaki, N. Nakada, T. Tsuchiyama, S. Takaki, Effect of grain size on thermal and mechanical stability of austenite in metastable austenitic stainless steel, ISIJ Int. 53 (2013) 1224–1230. https://doi.org/10.2355/isijinternational.53.1224.

[125] Z. Xie, Y. Wang, C. Lu, L. Dai, Sluggish hydrogen diffusion and hydrogen decreasing stacking fault energy in a high-entropy alloy, Mater. Today Commun. 26 (2021) 101902. https://doi.org/10.1016/j.mtcomm.2020.101902.

[126] G.B. Olson, M. Cohen, A general mechanism of martensitic nucleation: Part I. General concepts and the FCC→ HCP transformation, Metall. Trans. A. 7 (1976) 1897–1904.

[127] I.M. Robertson, The effect of hydrogen on dislocation dynamics, Eng. Fract. Mech. (1999). https://doi.org/10.1016/S0013-7944(99)00094-6.

[128] M. Koyama, S.M. Taheri-Mousavi, S.M. Taheri-Mousavi, H. Yan, J. Kim, B.C. Cameron, S.S. Moeini-Ardakani, J. Li, J. Li, C.C. Tasan, Origin of micrometer-scale dislocation motion during hydrogen desorption, Sci. Adv. 6 (2020). https://doi.org/10.1126/sciadv.aaz1187.

[129] M. Koyama, K. Tsuzaki, ε→γ Reverse Transformation-induced Hydrogen Desorption and Mn Effect on Hydrogen Uptake in Fe–Mn Binary Alloys, ISIJ Int. 55 (2015) 2269–2271. https://doi.org/10.2355/isijinternational.ISIJINT-2015-215.

[130] G.B. Olson, M. Cohen, A general mechanism of martensitic nucleation: Part I. General concepts and the FCC→HCP transformation, Metall. Trans. A. 7 (1976) 1897–1904. https://doi.org/10.1007/BF02654987.

[131] G. Xu, C. Wang, J.I. Beltrán, J. Llorca, Y. Cui, Landau modeling of dynamical nucleation of martensite at grain boundaries under local stress, Comput. Mater. Sci. 118 (2016) 103–111. https://doi.org/10.1016/j.commatsci.2016.02.042.

[132] S. Dash, N. Brown, Nucleation and growth of martensite in fe-32.3% Ni alloy, Acta Metall. 14 (1966) 595–603. https://doi.org/10.1016/0001-6160(66)90067-8.

[133] M. Ueda, H.Y. Yasuda, Y. Umakoshi, Controlling factor for nucleation of martensite at grain boundary in Fe-Ni bicrystals, Acta Mater. 51 (2003) 1007–1017. https://doi.org/10.1016/S1359-6454(02)00503-7.

[134] T. Song, B.C. De Cooman, Martensite nucleation at grain boundaries containing intrinsic grain boundary dislocations, ISIJ Int. 54 (2014) 2394–2403. https://doi.org/10.2355/isijinternational.54.2394.

[135] S. Mahajan, G.. Chin, Twin-slip, twin-twin and slip-twin interactions in Co-8 wt.% Fe alloy single crystals, Acta Metall. 21 (1973) 173–179. https://doi.org/10.1016/0001-6160(73)90059-X.

[136] J.W. Christian, S. Mahajan, Deformation twinning, Prog. Mater. Sci. 39 (1995) 1–157. https://doi.org/10.1016/0079-6425(94)00007-7.

[137] I.J. Beyerlein, X. Zhang, A. Misra, Growth Twins and Deformation Twins in Metals, Annu. Rev. Mater. Res. 44 (2014) 329–363. https://doi.org/10.1146/annurev-matsci-070813-113304.

[138] A. Serra, D.J. Bacon, A new model for (1012) twin growth in hcp metals, Philos. Mag. A Phys. Condens. Matter, Struct. Defects Mech. Prop. 73 (1996) 333–343. https://doi.org/10.1080/01418619608244386.

[139] S. Jiang, Z. Jiang, Q. Chen, Deformation twinning mechanism in hexagonal-close-packed crystals, Sci. Rep. 9 (2019) 1–5. https://doi.org/10.1038/s41598-018-37067-8.

[140] M.H. Yoo, J.K. Lee, Deformation twinning in h.c.p. metals and alloys, Philos. Mag. A Phys. Condens. Matter, Struct. Defects Mech. Prop. 63 (1991) 987–1000. https://doi.org/10.1080/01418619108213931.

[141] N. Narita, C.J. Altstetter, H.K. Birnbaum, Hydrogen-Related Phase Transformations in Austenitic Stainless Steels., Metall. Trans. A, Phys. Metall. Mater. Sci. 13 A (1982) 1355–1365. https://doi.org/10.1007/BF02642872.

[142] J. Kim, E. Plancher, C.C. Tasan, Hydrogenation-induced lattice expansion and its effects on hydrogen diffusion and damage in Ti-6Al-4V, Acta Mater. 188 (2020) 686–696.

https://doi.org/10.1016/j.actamat.2020.02.029.

[143] H. Pfeiffer, H. Peisl, Lattice expansion of niobium and tantalum due to dissolved hydrogen and deuterium, Phys. Lett. A. 60 (1977) 363–364. https://doi.org/10.1016/0375-9601(77)90129-3.

[144] M.E. Armacanqui, R.A. Oriani, Lattice expansion and contraction in sputtered metal films due to hydrogen charging, Mater. Sci. Eng. 92 (1987) 127–132. https://doi.org/10.1016/0025-5416(87)90162-5.

[145] M. Gong, J.P. Hirth, Y. Liu, Y. Shen, J. Wang, Interface structures and twinning mechanisms of twins in hexagonal metals, Mater. Res. Lett. 5 (2017) 449–464. https://doi.org/10.1080/21663831.2017.1336496.

[146] B. Li, E. Ma, Zonal dislocations mediating {1 0 -1 1}〈1 0 -1 -2〉 twinning in magnesium, Acta Mater. 57 (2009) 1734–1743. https://doi.org/10.1016/j.actamat.2008.12.016.

[147] E.G. Astafurova, G.G. Zakharova, H.J. Maier, Hydrogen-induced twinning in 〈0 0 1〉 Hadfield steel single crystals, Scr. Mater. 63 (2010) 1189–1192. https://doi.org/10.1016/j.scriptamat.2010.08.029.

[148] I. V. Kireeva, Y.I. Chumlyakov, A. V. Tverskov, H. Maier, Effect of hydrogen on orientation dependence of critical shear stress and mechanism of straining in single crystals of stable stainless steel, Tech. Phys. Lett. (2011). https://doi.org/10.1134/S1063785011060071.

[149] C. Hwang, I.M. Bernstein, Hydrogen induced slip and twinning in iron alloys, Scr. Metall. 16 (1982) 85–90. https://doi.org/10.1016/0036-9748(82)90408-2.

[150] K. Lublinska, A. Szummer, K.J. Kurzydlowski, Hydrogen induced microtwins in Cr alloyed ferrite, in: NATO Sci. Peace Secur. Ser. C Environ. Secur., Springer Verlag, 2008: pp. 757–764. https://doi.org/10.1007/978-1-4020-8898-8_95.

[151] K. Lublinska, A. Szummer, K.J. Kurzydlowski, An in situ investigation of the effect of hydrogen on ferritic stainless steel, Int. J. Nucl. Hydrog. Prod. Appl. 1 (2008) 324. https://doi.org/10.1504/ijnhpa.2008.023106.

[152] J.M. Rigsbee, R.B. Benson, A TEM investigation of hydrogen-induced deformation twinning and associated martensitic phases in 304-type stainless steel, J. Mater. Sci. (1977). https://doi.org/10.1007/BF00566284.

[153] J. Yamabe, T. Matsumoto, S. Matsuoka, Y. Murakami, A new mechanism in hydrogen-enhanced fatigue crack growth behavior of a 1900-MPa-class high-strength steel, Int. J. Fract. 177 (2012) 141–162. https://doi.org/10.1007/s10704-012-9760-9.

[154] Z. Li, F. Körmann, B. Grabowski, J. Neugebauer, D. Raabe, Ab initio assisted design of quinary dual-phase high-entropy alloys with transformation-induced plasticity, Acta Mater. 136 (2017) 262–270. https://doi.org/10.1016/j.actamat.2017.07.023.

[155] M. Nagumo, Fundamentals of hydrogen embrittlement, Singapore, 2016. https://doi.org/10.1007/978-981-10-0161-1.

[156] M.R. Ronchi, H. Yan, C.C. Tasan, Hydrogen-induced martensitic transformation and twinning in Fe45Mn35Cr10Co10, (2021).